# Validation for Global Solar Wind Prediction Using Ulysses Comparison: Multiple Coronal and Heliospheric Models Installed at the Community Coordinated Modeling Center

L.K. Jian (1,2), P.J. MacNeice (2), M.L. Mays (3,2), A. Taktakishvili (3,2), D. Odstrcil (4,2), B. Jackson (5), H.-S. Yu (5), P. Riley (6), I.V. Sokolov (7)

1. Department of Astronomy, University of Maryland, College Park, Maryland, USA
2. Heliophysics Science Division, NASA Goddard Space Flight Center, Greenbelt, Maryland, USA
3. Department of Physics, Catholic University of America, Washington, District of Columbia, USA
4. School of Physics, Astronomy, and Computational Sciences, George Mason University, Fairfax, Virginia, USA
5. Center for Astrophysics and Space Sciences, University of California, San Diego, La Jolla, California, USA
6. Predictive Science Inc., San Diego, California, USA
7. Department of Atmospheirc, Oceanic, and Space Sciences, University of Michigan, Ann Arbor, Michigan, USA



Abstract

The prediction of the background global solar wind is a necessary part of space weather forecasting. Several coronal and heliospheric models have been installed and/or recently upgraded at the Community Coordinated Modeling Center (CCMC), including the Wang-Sheely-Arge (WSA)-Enlil model, MHD-Around-a-Sphere (MAS)-Enlil model, Space Weather Modeling Framework (SWMF), and heliospheric tomography using interplanetary scintillation (IPS) data. Ulysses recorded the last fast latitudinal scan from southern to northern poles in 2007. By comparing the modeling results with Ulysses observations over seven Carrington rotations, we have extended our third-party validation from the previous near-Earth solar wind to mid-to-high latitudes, in the same late declining phase of solar cycle 23. Besides visual comparison, we have quantitatively assessed the models' capabilities in reproducing the time series, statistics, and latitudinal variations of solar wind parameters for a specific range of model parameter settings, inputs, and grid configurations available at CCMC. The WSA-Enlil model results vary

This is the author manuscript accepted for publication and has undergone full peer review but has not been through the copyediting, typesetting, pagination and proofreading process, which may lead to differences between this version and the Version of Record. Please cite this article as doi: 10.1002/2016SW001435

with three different magnetogram input. The MAS-Enlil model captures the solar wind parameters well, despite its underestimation of the speed at mid-to-high latitudes. The new version of SWMF misses many solar wind variations probably because it uses lower grid resolution than other models. The IPS-Tomography cannot capture the latitudinal variations of solar wind well yet. Because the model performance varies with parameter settings which are optimized for different epochs or flow states, the performance metric study provided here can serve as a template that researchers can use to validate the models for the time periods and conditions of interest to them.



## 1. Introduction

As a multiagency partnership, the Community Coordinated Modeling Center (CCMC, see http://ccmc.gsfc.nasa.gov/) hosts a variety of models extending from the solar surface to the Earth's ionosphere, and also provides a Run-on-Request (RoR) service of these models to the public. As an outsider of the modeling teams, a user is often left wondering about the reliability of these models and which one to choose. Even a member of a particular modeling team would be curious about how well other models perform. Therefore, it is necessary to have consistent validation of these models performed by a third party.

Coronal and heliospheric models are at the forefront of space weather forecasting. Successful predictions of the corona and solar wind background are a precondition for capturing transient events from the Sun [e.g., *Odstrčil and Pizzo*, 1999a, 1999b; *Vandas and Odstrčil*, 2000; *Case et al*., 2008; *Gopalswamy et al*., 2009; *Manchester et al*., 2014]. For example, a more massive solar wind would cause larger deceleration of coronal mass ejections (CMEs). Solar wind density, temperature, and interplanetary magnetic field (IMF) strength all contribute to the characteristic speeds, and thus are important for getting the right shock parameters, which are needed in solar energetic particle acceleration models [e.g., *Bain et al*., 2016]. Besides numerous validation efforts in each modeling team, there has been some third-party validation for the quasi-steady solar wind, e.g., *Owens et al*. [2005, 2008], *Lee et al*. [2009], *MacNeice* [2009a, b], and *Jian et al*. [2011a]. However, they validated mainly three models. The inter-comparison between more models only became available after more coronal and heliospheric models were installed at the CCMC and *Jian et al*. [2015] validated them for the solar wind prediction at Earth. To assess the modeling of global solar wind structure, a comparison with in situ observation far from the ecliptic plane is needed.

1.1. Ulysses Observation

NASA and ESA's joint Ulysses mission [*Wenzel et al*., 1992] is the only heliospheric mission which has ever measured the solar wind at mid-to-high latitudes continuously within 6 AU. Ulysses finished nearly three highly eccentric orbits around the Sun during its 18-year mission time, and Ulysses data has been used in many model developments [e.g., *Guhathakurta et al*., 1999; *Usmanov et al*., 2000; *Riley et al*., 2001a; *Aibéo et al*., 2007; *Oran et al*., 2013]. Because the synoptic magnetograms from the Global Oscillation Network Group (GONG) [*Harvey et al*., 1996], the most widely accepted input for models installed at the CCMC, became available in late 2006, Ulysses' fast latitudinal scan in 2007 is the appropriate time for this model validation. In addition, 2007 is in the late declining phase of solar cycle 23 before reaching the deep solar minimum [e.g., *Gibson et al*., 2011; *Jian et al*., 2011b]. The solar wind encountered by Ulysses is dominated by quasi-steady structures with only one slow interplanetary CME (on days 185-186).

Ulysses orbit in 2007 is shown in Figure 1. In the heliographic inertial (HGI) coordinate system, the X-axis is directed along the intersection line of the ecliptic and solar equatorial planes, the Z-axis is directed perpendicular to and northward of the solar equator, and the Y-axis completes the right-handed set. Because of poor solar magnetic field observation in the polar region, the Enlil model at the CCMC, by default, provides the solar wind simulation only within $\pm 60^{o}$ in latitude, although it can, in principle, model the solar wind up to higher latitudes. On the other hand, the interplanetary scintillation (IPS) observations at high latitudes are coarse and generally obtained close to the solar surface where the polar wind can be highly variable at solar minimum [*Jackson et al*., 2014; *Yu et al*., 2016], requiring averaging not yet available in the time-dependent tomography. Thus, we limit the comparison with Ulysses data in Carrington rotations (CRs) 2056-2062, as in *Jian et al*. [2015]. Considering the solar wind propagation time, we start from day 123, which is six days later than the official start time of CR 2056 for synoptic maps of photospheric magnetograms. Because the evolution speed at Ulysses orbit is slightly slower than at Earth, we use 27 days as an approximated CR period. Hence, the CRs 2056-2062 correspond to days 123-312 in 2007.

1.2. Introduction of Models and Synoptic Map Input

Figure 2 outlines the couplings of photospheric magnetograms, coronal and heliospheric models to be validated in this study. There are two coronal models coupled with the Enlil heliospheric model [e.g., *Odstrčil*, 1994; *Odstrčil et al*., 1996; *Odstrčil and Pizzo*, 1999a]: the MHD-Around-a-Sphere (MAS) model from Predictive Science Inc. [e.g., *Mikić and Linker*, 1994, 1996; *Linker*

*et al.*, 1996, 2003; *Riley et al.*, 2001a, 2001b; *Lionello et al*., 2009] and the Wang-Sheeley-Arge (WSA) model from the Air Force Research Laboratory [e.g., *Wang and Sheeley*, 1990a, 1990b, 1992; *Arge and Pizzo*, 2000; *Arge et al.*, 2002]. In addition, there are two models extending from the corona to the heliosphere: the solar corona and inner heliospheric parts of the Space Weather Modeling Framework (SWMF) from the University of Michigan [e.g., *Tóth et al.*, 2005, 2012; *van der Holst et al.*, 2010, 2014; *Sokolov et al.*, 2013], and the heliospheric tomography from the University of California, San Diego (UCSD) using IPS data [e.g., *Hewish et al*., 1964; *Coles*, 1978; *Jackson et al*., 1997, 1998, 2011]. The runs of coupled MAS and Enlil models are requested at the CORona-HELiosphere (CORHEL) module at CCMC. The previous version v4.7 is no longer run at CCMC, so we only consider the latest v5.0 (available since 2014). There are two types of MAS coronal model, one with polytropic implementation, and the other with full thermodynamic energy equation. For the SWMF, there are two versions still running at CCMC: v8.03 and v9.20 available since 2012 and 2014, respectively. The latter is also known as Alfvén-Wave driven SOlar wind Model (AWSoM) [*van der Holst et al.*, 2014]. An extensive model introduction, including the differences in various versions, was made in section 2 of *Jian et al*. [2015], so we do not repeat it in this accompanying study. Instead we provide brief descriptions of the model, grid resolution, and inner boundary condition in Table 1.

At the CCMC, the default input for quasi-steady solar wind simulation is integral fully-calibrated CR synoptic magnetograms. Different models can use maps from different sources. The magnetograms from the Michelson Doppler Imager (MDI) [*Scherrer et al*., 1995] can be used as input for the MAS model, but not used for the WSA or SWMF models at the CCMC yet. Because GONG is most widely accepted by the coronal models, we use it as the common input for the models. To evaluate the effect of different magnetogram input on the same model, we also use National Solar Observatory (NSO) Synoptic Optical Long-term Investigation of the Sun (SOLIS) at Kitt Peak in Arizona [*Pierce*, 1969], and Mount Wilson Observatory (MWO) [*Ulrich et al*., 2002] synoptic magnetograms as input to the WSA-Enlil model. Note “NSO” is used to stand for NSO/SOLIS thereafter.

### 1.3. New Version of Enlil Model

As shown in *Jian et al*. [2015], the magnetic field and solar wind temperature from Enlil v2.7 are much lower than observed. This was done deliberately to enhance system robustness because Enlil v2.7 was delivered to NOAA Space Weather Prediction Center for operational use just before this solar maximum. The parameter setting producing weaker magnetic field and lower temperature would lower the characteristic speeds at the inner boundary of Enlil and thus ensure

boundary conditions with super-critical outflow. After many more tests for the solar maximum, Dr. Odstrcil became more confident that a different setting producing stronger magnetic field and higher temperature would still work even in the cases of strong and multiple CMEs. Thus, Enlil v2.8 became available for RoR at CCMC in late 2015 and it is coupled with WSA coronal model, but not with MAS model yet. Figure 3 illustrates the different performance of Enlil v2.7 vs. v2.8 with the same GONG magnetogram input and same WSA v2.2 coronal model. In contrast with v2.7, the new model provides faster fast wind and a larger difference between slow and fast wind, more closely matching the Ulysses observation. Enlil v2.8 also produces stronger IMF and hotter solar wind, closer to observation, attributed to the increased magnetic field scaling factor and added heating.

1.4. Model Coupling and Data Processing for Validation

In this paper, as indicated in Figure 2, we validate the following models: (1) the WSA v2.2 coronal part + Enlil model v2.8 (in short, WSA-Enlil), (2) the MAS v5.0 coronal part + Enlil model v2.7 (in short, MAS-Enlil), (3) the SWMF, and (4) the heliospheric tomography v15 using IPS data (in short, IPS-Tomography). The IPS time dependent tomography does not need the magnetic field maps to provide solar wind speed and density and it is not designed to be a background solar wind model. It gets the GONG magnetogram data every 6 h (to match with tomography cadence) using the Current-Sheet Source Surface (CSSS) model [*Zhao and Hoeksema*, 1995] and convects the magnetic field outward to provide radial and azimuthal components. Hence, the connection between GONG and IPS-Tomography in Figure 2 is marked by a dashed arrow line, and GONG is not mentioned when presenting IPS-Tomography results in the following, except when discussing the magnetic field polarity.

The MAS/WSA-Enlil model and SWMF installed at the CCMC output the solar wind plasma as well as the IMF and its polarity at the orbits of planets and major spacecraft within 2 AU, including the pertinent orbit of Ulysses. IPS-Tomography results at Ulysses are provided directly by the modeling group, because the output at planets and spacecraft has not been made available in a digital format at the CCMC [*Jian et al*., 2015]. The same model is run in exactly the same way at UCSD and provides digital data for real-time predictions. The tomography results are interpolated into hourly data for comparison.

The model resolutions and inner boundary conditions are listed in Table 1. Using an approximate solar rotation period of 27 days, a longitudinal resolution of 2.5$^{o}$ corresponds to 4.5 h in time. Using a solar wind speed of 400 km/s, a radial resolution of 1 Rs in the heliospheric model corresponds to 0.48 h in time. The coarsest radial scale among Enlil coupled with WSA/MAS

and SWMF is 8 Rs, corresponding to about 4 h. In order to match with the actual coarse resolution from models (see section 3 of *Jian et al*. [2015] for detail), we use hourly Ulysses data and conduct a 5h moving (boxcar) averaging centered at the current data point.

As in *Jian et al*. [2015], the following four basic solar wind parameters are used to assess the model performance: solar wind speed V, proton number density Np, magnetic field intensity B, and proton temperature Tp. In section 2 we illustrate the variability of the model performance in reproducing these parameters and conduct a visual inspection. In section 3 we calculate the root mean square error (RMSE) using the time series of solar wind parameters and compare the above models along with three persistence models. In section 4 we compare the correlation between the observed and predicted solar wind parameters from different models. The capabilities in capturing the latitudinal variations of solar wind are evaluated in section 5. The performance in reproducing the solar wind statistics at low latitudes and mid-to-high latitudes are assessed in section 6. Because there are no global and few local measures of any of the flow variables (V, Np, B, and Tp) driving the solar wind, all the near-Sun input has to be parameterized in some sense. All models are necessarily rife with auxiliary internal parameters. We devote section 7 to discuss the effects of different parameter settings and different versions of GONG magnetogram synoptic maps. We finally discuss and conclude in section 8.

## 2. Visual Comparison

Figures 4 – 7 illustrate the comparison between Ulysses observations (enclosed by a black box in the center) and model results of V, Np, B, and Tp, respectively. Each block is composed of stacked panels of seven CRs. The abscissa indicates the day of each CR, and the ordinate is CR 2056 to 2062, corresponding to a latitudinal change from $60^o$ south to $60^o$ north. The figures demonstrate the great variability of the models' capabilities in reproducing these solar wind parameters.

From Figure 4, it is clear that the solar wind speed in the first and last two CRs, i.e., at mid-to-high latitudes ($30^o$-$60^o$ south and north in Figure 1) is underestimated by GONG-MAS v5.0-Enlil v2.7 (more in Figure 9). The solar wind speed from IPS-Tomography is more variable than observed in the first and last two CRs, perhaps partly because IPS signals at these latitudes are coarse and sensitive to polar wind dynamics near the solar surface.

Figure 5 illustrates the comparison for Np, which varies considerably along Ulysses orbit and so is plotted on a logarithmic scale. The IPS-Tomography results do not show the expected latitudinal variation of Np. GONG-SMWF v9.20 underestimates the observed Np most in the

first and last two CRs, in each case by more than 50% (Figure 15). As listed in Table 1, for the inner boundary at a similar region (top of chromosphere), the physics-based MAS v5.0 Thermodynamic, SWMF v8.03, and SWMF v9.20 models set the temperature and density differently. More investigation is needed to determine why the density from SWMF v9.20 is too low.

IPS-Tomography does not currently provide B or Tp. All the remaining models underestimate B somewhat, as demonstrated in Figure 6. The underestimations from the MWO/NSO–WSA v2.2–Enlil v2.8 are relatively small. The underestimation in GONG– MAS v5.0–Enlil v2.7 is expected to be easily fixed by increasing the scaling factor of B as in Enlil v2.8.

All the models underestimate Tp in the first and last two CRs except GONG-SWMF v9.20, as displayed in Figure 7. This suggests the implementation of Alfvén wave and turbulence heating in the new version of SWMF really works in the right direction of getting hotter solar wind. The Enlil model does not separate electron and proton temperature, so its result should be compared with their average. However, the electron temperature is not available from Ulysses for this period. In the fast latitude scan of Ulysses in 1994-1995, the core electron temperature is generally lower than $1.5\times10^5$K, while the halo electron temperature is 4-8 $\times10^5$K [e.g., *Issautier et al*., 2001]. If using the core electron temperature, the temperature produced by the Enlil model may not be that different from the average plasma temperature. After this visual inspection, quantitative comparison is conducted in the following four sections.

## 3. Validation for Time Series of Solar Wind Parameters

*Jian et al.* [2015] used the mean-square-error (MSE) to assess the match between the modeled and observed time series of solar wind parameters. MSE is useful but cannot directly present the difference between the modeled and observed values. Thus, we use the root mean square error (RMSE) here. For a time series of a parameter $x(t)$,

$$\mathrm{RMSE} = \sqrt{\frac{1}{n}\sum_{t=1}^{n}[x_{modeled}(t) - x_{observed}(t)]^2}.$$

In order to remove the discrepancy caused by the parameter averages between simulation and observation, we also first normalize the solar wind parameter by its average in each CR and then calculate the RMSE. Figure 8 (A) and (B) show the RMSEs of solar wind parameters without and with normalization, respectively. The higher the bar, the larger the RMSE, the lower is the

ranking given at the bottom of each panel, and the worse the modeled time series match with observation.

Additionally, following *MacNeice* [2009b] and *Jian et al*. [2015], we add some persistence models as benchmarks to assess any benefit of these complicated models in Figure 2. Because Ulysses orbit changes considerably from one CR to the next as shown in Figure 1, we do not include a persistence model using observations taken one CR ahead. We choose the persistence models using the in situ observations taken one, two, or three days ago, i.e., 1-day, 2-day, 3-day persistence models.

From Figure 8 (A), the 1-day and 2-day persistence models capture the time series of V and Tp best, but they have a shorter warning time than models using magnetogram input. Among the models installed at CCMC, called "CCMC models" hereafter, the GONG–MAS v5.0 Polytropic–Enlil v2.7 and GONG-WSA v2.2-Enlil v2.8 models match with time series of V relatively well, while the GONG-SWMF v9.20 and GONG–MAS v5.0 Polytropic–Enlil v2.7 model match with time series of Tp relatively well. The GONG-SWMF v9.20 and IPS-Tomography mismatch with the time series of V most. For Np, the MWO-WSA v2.2-Enlil v2.8 model works best, even better than 1-day persistence model. The GONG-SWMF v8.03 is the most poorly matched with the time series of Np, probably because it largely overestimates Np (see Figures 14 and 15). For B, the WSA v2.2-Enlil v2.8 model using magnetograms from three different sources works slightly better than other CCMC models, probably due to the increased scaling factor of B in Enlil v2.8.

As illustrated in Figure 8 (B), the rankings change substantially for the RMSEs of normalized solar wind parameters. The strengths of persistence models are weakened. In contrast to Figure 8 (A), the 1-day persistence model works best only for the time series of normalized V. Among the CCMC models, the GONG–MAS v5.0 Polytropic–Enlil v2.7 model matches best with normalized V, Np, and Tp. The WSA v2.2–Enlil v2.8 model using MWO magnetogram matches all four normalized parameters better than when using GONG or NSO/SOLIS magnetogram. The GONG-SWMF v8.03 has larger RMSEs for normalized Np, B, and Tp than GONG-SWMF v9.20, although it can produce higher order of variations in the solar wind than the smoothed version from GONG-SWMF v9.20 (Figures 4-7). The MWO-WSA v2.2-Enlil v2.8 model has the highest RMSE for Tp, but the second lowest RMSE for normalized Tp. The remarkable differences between Figure 8 (A) and (B) indicate the necessity of removing the biases of averages when evaluating the time variations.

4. Correlation between Modeled and Observed Solar Wind Parameters

Next, we assess the model performance using the Pearson correlation between modeled and observed solar wind parameters. Figures 9-12 display the occurrence distributions of all the pertinent models for V, Np, B, and Tp, respectively. The abscissa denotes the observed parameter, while the ordinate marks the modeled parameter with the same range. The correlation coefficient between the observed and modeled parameters is given at the top of each panel. Because there are 4537 samples in each data set for each parameter, the probability of getting the lowest listed correlation of 0.08 by random chance (the p-value) is nearly 1 out of 10 million, thus the listed correlation is significant. The persistence models using the same Ulysses data are expected to match well with observed solar wind statistics, thus we do not consider them in this section.

For all four solar wind parameters, the GONG–MAS v5.0–Enlil v2.7 model has the top two correlation coefficients with Ulysses observations among all CCMC models, generally the highest from the polytropic version, while the second (if not equally first) from the thermodynamic version. However, all the GONG – MAS v5.0 (polytropic and thermodynamic) – Enlil models generate maximum speeds of about 686 km/s, which is more than 100 km/s slower than the observed fastest solar wind. This upper limit of V output is perhaps due to the default fast-wind speed of 650 km/s used in the ad hoc correction at the outer boundary (30 solar radii) of the MAS coronal model [*Riley et al*., 2001a, 2001b]. We may get faster solar wind to match with Ulysses observation by setting a higher default value when requesting the MAS-Enlil runs at the CCMC, but it may affect the match with the maximum speed at Earth [*Jian et al*., 2015] and the solar wind dynamics in general. In contrast to the best correlation near Earth in *Jian et al*. [2015], IPS Tomography v15 has the lowest correlation coefficients with the observed V and Np at Ulysses orbit among all CCMC models. The GONG-WSA v2.2-Enlil v2.8 model is correlated with observed V second best to the GONG–MAS v5.0–Enlil v2.7 model. For Np and B, the model with the third highest correlation coefficient is MWO-WSA v2.2-Enlil v2.8. Although GONG-SWMF v9.20 only provides smoothed results, the Np, B, and Tp from it correlate with observations better than GONG-SWMF v8.03.

## 5. Validation for Latitudinal Variations of Solar Wind

As displayed in Figure 1, from CR 2056 to 2062, Ulysses flew quickly from -60$^o$ (south) to 60$^o$ (north) in latitude, while the heliocentric distance did not change much from 1.4 to 1.8 AU. To emphasize the latitudinal variation of solar wind, we plot the solar wind speed (blue line) vs. heliographic latitude in Figure 13. The near-Earth solar wind prediction validated in *Jian et al*. [2015] covers only from -4$^o$ to 7$^o$ in latitude during the same time period. Highly variable solar

wind featured by the switches between slow and fast wind streams in fact extends to about ±30$^o$, as shown in the Ulysses observation, marked in the red box. This range should roughly correspond to the solar wind from the helmet streamers or pseudostreamers. The models generally capture the variability of solar wind within ±30$^o$ with the exception of the GONG-SWMF v9.20. Because of higher grid resolutions in the heliospheric part (see Table 1), the WSA v2.2-Enlil v2.8 model captures more small variations of V than the MAS v5.0-Enlil v2.7 model using the same GONG magnetogram.

Another way to describe the low-latitude region is to use the magnetic field polarity, which can be approximated by the sign of the radial field, -1 for inward, 1 for outward. The magnetic field sectors are filtered to eliminate transient (<1 day) field changes using the six-step algorithm elaborated in section 7 of *Jian et al*. [2015]. In Figure 13, the orange lines draw the latitudinal variations of magnetic field polarity. One change of the magnetic field polarity marks a crossing of the sector boundary. Except for a couple of transient crossings, most of the sector boundary crossings in Ulysses observations are well captured by all these models except the GONG-SWMF v9.20. The GONG-SWMF v9.20 also generates a greater asymmetry between northern and southern hemispheres than observed. This model produces faster solar wind in the southern hemisphere and locates the sector boundary crossing at about 10$^o$ south. The magnetic field polarity from IPS-Tomography v15 using GONG synoptic maps every 6 h and the CSSS model is nearly the same as the polarity from other model couplings using CR synoptic map and the Potential-Field Source Surface (PFSS) model [*Altschuler and Newkirk*, 1969; *Schatten et al*., 1969].

## 6. Validation for Solar Wind Statistics in Two Regions

To evaluate the models' capabilities in reproducing the statistics of solar wind parameters, we calculate the ratios of the modeled to observed parameters. As suggested by the analysis above, we divide the solar wind into two regions: low latitudes (within ±30$^o$), and mid-to-high latitudes (30$^o$-60$^o$ in each hemisphere). Figures 14 and 15 show the modeled/observed ratios of solar wind parameters for these two regions, respectively. The results using mean or median values are similar, especially for the mid-to-high latitude solar wind. Therefore in the following discussion we use only the median.

As shown in Figure 14, the predicted median V at low latitudes is in the range of ±25% around the observed median. All the models capture the observed median V well, except for the overestimation by IPS-Tomography v15. For the median Np, the WSA v2.2-Enlil v2.8 model best matches observation, regardless of photospheric magnetogram input, while the other models

generally overestimate it, some by a factor of 2. Note however, that the proton densities can differ by as much as a factor of two from instrument to instrument. Although there is no such issue in this study, it could be a problem for model validations using densities from multiple observation sources. Some models (e.g., IPS-Tomography) have optimized different settings for comparing with different data.

All the models underestimate the median B, except MWO/NSO-WSA v2.2-Enlil v2.8. All the models underestimate the median Tp, especially the GONG–MAS v5.0 Thermodynamic–Enlil v2.7 and GONG-SWMF v8.03 models which do so by about 60%. However, their synthesized EUV images match very well with the coronal observation [e.g., *Lionello et al*., 2009; *van der Holst et al*., 2014], which is almost impossible to achieve using the semi-empirical WSA model and IPS-Tomography.

For the mid-to-high latitude solar wind, the median V predicted by models is within ±20% of the observation, as illustrated in Figure 15. The models capture the median V well, except for the GONG-SWMF v9.20 and IPS-Tomography v15. For the median Np, all the WAS/MAS-Enlil models overestimate it slightly, while the GONG-SWMF v8.03 overestimates it by a factor of 2 and IPS-Tomography v15 by a factor of 3.4. The GONG-SWMF v9.20 underestimates the median Np by 65% (also shown in Figure 5). All the models underestimate the median B at mid-to-high latitudes, by about 20-84%, by the least for MWO/NSO-WSA v2.2-Enlil v2.8, and the most for the GONG-MAS v5.0-Enlil v2.7 model. An increase of the scaling factor could fix this. Except for GONG-SWMF v9.20, all the models underestimate the median Tp by 50-60%.

## 7. The Effect of Magnetogram Input and Parameter Setting

There are three types of synoptic magnetograms in the GONG archive (http://gong2.nso.edu/archive/patch.pl?menutype=s): the standard quick-reduce magnetogram ("mrbqs" in the file name, which is the default input for RoR of CME simulations at the CCMC), the standard quick-reduce zero point corrected magnetogram ("mrzqs" in the file name), and the integral CR magnetogram ("mrmqs" in the file name, which is the default input for RoR of steady solar wind simulations at the CCMC). The quick-reduce zero point correction was developed during solar minimum 23/24, and it is still under review because of the questionable behavior during the recent polar field reversal, thus it cannot be applied to the fully-calibrated CR maps without more research and development as well as computational resources (Gordon Petrie, personal communication in 2015). The PFSS model results provided by NSO/SOLIS are not based on zero point corrected magnetograms either. Because the whole situation of synoptic solar magnetogram is not yet optimal, we use the integral CR magnetogram from GONG without

zero point correction (default at the CCMC) in sections 2-6, and test the effect of the correction in this section.

It is possible, by special request, to run WSA v2.2-Enlil v2.8 model at CCMC using time-dependent synoptic maps of magnetograms at any time frequency. Because the investigation period is as long as 162 days, we have run the model using two types (without and with zero point correction) of daily updated GONG maps to compare with the results using CR synoptic maps. In addition, through special request, we also test the effect of an alternative parameter setting (a6b1), which is possibly to be implemented at CCMC in the near future.

Figures 16-18 illustrates the different performance of WSA v2.2-Enlil v2.8 using three types of GONG magnetograms and two types of parameter settings in capturing V, Np, and B, respectively. Top rows use the same present parameter setting (a4b1). Because seven runs are needed for CR-synoptic maps, the alternative setting is not requested for them. In contrast with the maps without zero point correction, the runs using corrected maps generate slightly slower fast wind and weaker B, mismatching with observations more, possibly because the model setting is not optimized for corrected maps. In contrast with the runs using the present setting, the runs using the alternative setting generate lower Np and stronger B, consistent with the decrease of number density (from 200 to 125 $cm^{-3}$) and the increase of B scaling factor (from 2 to 4) in the alternative setting. The resultant comparison with Ulysses observation is mixed, with one improvement and one deterioration.

Figure 19 displays the performance in capturing the IMF inward/outward polarity (between $60^o$ south to $60^o$ north) of the GONG-WSA v2.2-Enlil v2.8 model using the present setting and three different synoptic magnetogram maps. Comparison is made both without IMF sector grouping (the shortest sector is 1 h), and with IMF sector grouping (the shortest sector is 1 day). The runs using daily magnetograms do not capture many more transient sectors than the one using CR synoptic map, partly because the magnetogram has been smoothed to $2.5^o$ (~4.5 h) for the WSA coronal model. However, some of the sectors longer than 4.5 h are not captured using the daily maps either. The multiple sectors in CR 2059 are better captured by the run using CR maps, while the short outward sector in CR 2060 is better captured by the run using daily maps. This suggests that there is no superior one among the three types of GONG magnetograms for capturing IMF polarity in this period.

Figure 20 shows the RMSEs of solar wind parameters from the five different runs. No particular run has the lowest RMSEs for all the parameters. The difference in RMSE among them can be comparable with the ones from different model couplings in Figure 8 (A), indicating the large

influence of the parameter setting and/or magnetogram input. Without sufficient measures near the Sun, many parameters are used to set boundary conditions for models, such as the clipping and expansion of velocity and density ranges, the correlations imposed among the parameters, the corrections and adjustments for the too-weak magnetic fields from synoptic maps, the angular offsets to allow for the lack of rotation in the near-Sun portions of some models, etc. Some of the parameter settings have recently been provided as control files in the run result page at CCMC, and some of the parameters can be adjusted by special request. Thus, users can delve into the internal parameter issues if needed.

In addition, the parameter settings used in the models are often optimized for specific flow states and epochs, which can vary largely across models. For example, the combinations that appear relevant at solar minimum may be inappropriate at solar maximum, and they may also change from one minimum/maximum to the next one. Thus, we emphasize the present validation results only refer to the default settings at CCMC and to the particular time period near last solar minimum 23/24.

## 8. Conclusions and Discussion

Enlil v2.8 was installed at CCMC in late 2015. We have comprehensively validated the coronal and heliospheric models available for RoR at CCMC, by comparing with Ulysses observation from $60^o$ south to $60^o$ north of the solar equatorial plane in 2007. The results using visual inspection, RMSEs, correlation coefficients, and modeled/observed ratios represent different aspects of the model performance and do not always rate the models the same. Thus we need to use all of them to build comprehensive performance metrics. To provide a reference for model developers and users, Table 2 summarizes the strengths and weaknesses of these models in terms of capturing the global solar wind structures in this particular half-year period of 2007. Each of the models makes a number of simplifying assumptions, even the synoptic photospheric magnetogram itself is generated by some modeling (see the discussion in section 7 and *Riley et al*. [2014]). Hence the differences between model performances may be largely due to how the assumptions in the models are met, how different models handle the input, and how different the model grid configurations are, rather than the physics used in the models.

According to RMSEs of solar wind parameters, the models installed at the CCMC can perform better than persistence models that use the in situ observations taken two to three days ago. If we normalize the solar wind parameters first, even the 1-day persistence model cannot perform as well as some of the CCMC models. Since it is hard to keep a solar wind monitor out of the ecliptic plane, even if there is one, it is only one-point observation, and because the mid-to-high

latitude solar wind always affects the CME and energetic particle propagation in the ecliptic plane, it is necessary and important to develop the models examined here.

The performance of the IPS-Tomography at Ulysses orbit is not nearly as good as at Earth. It generates too many transient structures in the solar wind (Figures 4 and 13) which are not observed by Ulysses especially above 30$^o$, therefore its predicted V and Np are not well correlated with the Ulysses observations. The numbers of IPS signals are limited out of the ecliptic plane at present. IPS observations over the north and south ecliptic poles are generally obtained close to the solar surface. Coronagraph and IPS studies suggest that the polar solar wind can be highly variable near the Sun at solar minimum [*Jackson et al*., 2014; *Yu et al*., 2016] requiring averaging not yet available in the time-dependent tomography.

The GONG-MAS v5.0-Enlil v2.7 model cannot generate the solar wind at mid-to-high latitudes that is as fast as observed, probably because the default fast wind speed at the interface of MAS and Enlil models (30 Rs) is not optimized for this region. Despite this drawback, the GONG-MAS v5.0 Polytropic-Enlil v2.7 model matches with the time series of V and normalized parameters best except for normalized B, and it correlates with all four solar wind parameters best; while the GONG-MAS v5.0 Thermodynamic-Enlil v2.7 model correlates with these parameters second best.

The WSA v2.2-Enlil v2.8 model matches well with median Np at all latitudes. Among the three different CR maps, the model runs using MWO and NSO/SOLIS match well with median B at all latitudes, while the one using GONG still underestimates B at all latitudes. This suggests that the new scaling factor of B in Enlil v2.8 is probably not high enough for GONG, at least for this period. The MWO-WSA v2.2-Enlil v2.8 model matches with the time series of Np and B best, but underestimates the fast wind speed above 30$^o$. In contrast, the NSO/SOLIS-WSA v2.2-Enlil v2.8 model reproduces low-latitude median B and Tp as well as high-latitude median V best, but mismatches with the time series of normalized V most. Although GONG-WSA v2.2-Enlil v2.8 does not perform best in any particular aspect, its performance is well-rounded with no major weakness, similar to the conclusion in *Jian et al*. [2015]. In short, the results are sensitive to the magnetogram input, and to the different versions (e.g., daily vs. CR, with vs. without zero point correction) of synoptic maps from the same source as shown in section 7.

The two versions of GONG-SWMF underestimate B at the high latitudes. The GONG-SWMF v8.03 mismatches with the time series of Np and normalized parameters most except for normalized V. The GONG-SWMF v9.20 presents a much smoothed solar wind, similar to Figure 17 in *Oran et al*. [2013], probably because the grid resolution is only 8 Rs at places away from

the heliospheric current sheet in a Cartesian grid for the heliospheric part (20-500 Rs). Because the model does not predict the latitudinal excursions of the slow wind and the current sheet remains unrealistically confined near the equator (Ward Manchester, personal communication in 2016), it misses solar wind variations and multiple sector boundary crossings at low latitudes, and yields stronger asymmetry between northern and southern hemispheres than observed. The model developers are currently working to address the problem. Nevertheless, it is the only model to reproduce the hot solar wind at high latitudes and it matches with the mean solar wind temperature best. In contrast with v8.03, SWMF v9.20 correlates better with the observed Np, B, and Tp, and also better matches their time series.

Many parameters are used in setting the models, and the difference caused by different settings can sometimes be as great as caused by using different model couplings, as shown in section 7 (e.g., Figures 20 vs. 8). The parameter settings are often optimized for specific epochs (e.g., solar minimum vs. solar maximum) or specific flow states (e.g., low latitude vs. high latitude; slow vs. fast wind) when they were developed, thus the model performance may vary greatly after it is delivered to CCMC and then validated for a different epoch and/or a different flow state. Therefore, the strengths and weaknesses diagnosed from *Jian et al*. [2015] and this study are by no means definite. In addition, the different inner boundary conditions and grid sizes used by different models (listed in Table 1) may also significantly affect the results. It is desirable to compare the different models using the same inner boundary conditions and the same grid sizes, options which may become available at the CCMC in the future. Nevertheless, this study and *Jian et al*. [2015] are essential for providing performance metrics and statistics, for near-Earth and global solar wind, respectively. We recommend model users be open-minded when using the models (especially for planetary studies for which close-by solar wind monitors are not available) and conduct their own comparison for the time periods and conditions of interest.

ESA's Solar Orbiter mission which is scheduled to launch in 2018 will view the Sun and monitor the solar wind from latitudes of up to 25-30$^{o}$ at its perihelion passes near 0.3 AU [e.g., *Müller et al*., 2013]. The Polarimetric and Helioseismic Imager [*Gandorfer et al*., 2011] onboard the spacecraft will provide high-resolution and full-disk measurements of the photospheric vector magnetic field, which will be important input for all the coronal models. This mission will also be a second chance after Ulysses to observe the solar wind out of the ecliptic plane and to validate the model performance in reproducing global heliospheric structures much closer to the Sun. From now to 2018, we expect more model development using a new Air Force Data Assimilative Photospheric Flux Transport [*Arge et al*., 2010, 2011, 2013] and the high-resolution photospheric observations from the Helioseismic and Magnetic Imager [*Scherrer et al*., 2012] of

the Solar Dynamics Observatory. Continuous model validation is needed in this development and will help the models to get ready for the research-to-operation transfer.

Acknowledgements

This work is supported by NSF grants AGS 1242798, 1321493 and 1259549. AT and IVS are supported by NSF grant AGS 1257519. Simulation results have been provided by the CCMC at NASA/GSFC through their public Runs on Request system (http://ccmc.gsfc.nasa.gov/requests/requests.php). The results of IPS tomography are available upon request from Prof. Bernard Jackson at the University of California, San Diego. The simulation results of other models are available to the public at http://ccmc.gsfc.nasa.gov/ungrouped/SH/Helio_main.php by searching "Jian" as run requestor's last name and choosing 2056 – 2062 as the Carrington rotation number. The CCMC is a multi-agency partnership between NASA, AFMC, AFOSR, AFRL, AFWA, NOAA, NSF, and ONR. We are grateful to the CCMC team for their work. We thank the GONG, MWO and NSO/SOLIS teams for providing the photospheric magnetograms. We appreciate all the modeling teams for providing their models at the CCMC and for their consultation. We are grateful to Dr. Ward Manchester for verifying the current version of SWMF/AWSoM at the University of Michigan performs the same as reported here at Ulysses orbit. LKJ thanks Rebekah M. Evans for running the SWMF v8.03 model in 2012. We acknowledge the Space Physics Data Facility at NASA/GSFC for providing Ulysses data (see http://omniweb.gsfc.nasa.gov/coho/).

References

Aibéo, A., J. J. G. Lima, and C. Sauty (2007), Application of a MHD hybrid solar wind model with latitudinal dependences to Ulysses data at minimum, A&A, 461, 685-694, doi: 10.1051/0004-6361:20065123.

Altschuler, M. A., and G. Newkirk, Jr. (1969), Magnetic fields and the structure of the solar corona, *Sol. Phys.*, *9*, 131-149, doi: 10.1007/BF00145734.

Arge, C. N., and V. J. Pizzo (2000), Improvement in the prediction of solar wind conditions using real-time solar magnetic field updates, *J. Geophys. Res.*, *105*, 10465-10479, doi: 10.1029/1999JA000262.

Arge, C. N., D. Odstrcil, V. J. Pizzo, and L. Mayer (2002), Improved method for specifying solar wind speed near the Sun, in *Solar Wind Ten*, *AIP Conf. Proc.*, vol. *679*, edited by M. Velli and R. Bruno, pp. 190-193, AIP, Melville, New York, doi: 10.1063/1.1618574.

Arge, C. N., C. J. Henney, J. Koller, C. R. Compeau, S. Young, D. MacKenzie, A. Fay, and J. W. Harvey (2010), Air Force Data Assimilative Photospheric Flux Transport (ADAPT) model, in *Solar Wind 12, AIP Conf. Proc.*, vol. *1216*, edited by M. Maksimovic, K. Issautier, N. Meyer-Vernet, M. Moncuquet, and F. Pantellini, pp. 343-346, AIP, Melville, New York, doi: 10.1063/1.3395870.

Arge, C. N., C. J. Henney, J. Koller, W. A. Toussaint, J. W. Harvey, and S. Young (2011), Improving data drivers for coronal and solar wind models, in *5th International Conference of Numerical Modeling of Space Plasma Flows: ASTRONUM-2010, ASP Conf. Ser.*, vol. *444*, edited by N.V. Pogorelov, E. Audit, and G.P. Zank, pp. 99-104, ASP, San Francisco, Calif.

Arge, C. N., C. J. Henney, I. G. Hernandez, W. A. Toussaint, J. Koller, and H. C. Godinez (2013), Modeling the corona and solar wind using ADAPT maps that include far-side observations, in *Solar Wind 13, AIP Conf. Proc.*, vol. *1539*, edited by G. P. Zank, J. Borovsky, R. Bruno et al., pp. 11-14, AIP, Melville, New York, doi: 10.1063/1.4810977.

Bain, H. M., M. L. Mays, J. G. Luhmann, Y. Li, L. K. Jian, and D. Odstrcil (2016), Shock connectivity in the 2010 August and 2012 July solar energetic particle events inferred from observations and ENLIL modeling, *Astrophys. J.*, *825*, 1, doi: 10.3847/0004-637X/825/1/1.

Case, A. W., H. E. Spence, M. J. Owens, P. Riley, and D. Odstrcil (2008), Ambient solar wind's effect on ICME transit time, *Geophys. Res. Lett.*, *35*, L15105, doi: 10.1029/2008GL034493.

Gibson, S. E., *et al*. (2011), The whole heliospheric interval in the context of a long and structured solar minimum: An overview from Sun to Earth, *Sol. Phys.*, *274*, 5-27, doi: 10.1007/s11207-011-9921-4.

Coles, W. A. (1978), Interplanetary scintillation, *Space Sci. Rev.*, *21*, 411-425, doi: 10.1007/BF00173067.

Gandorfer, A., *et al*. (2011), The Solar Orbiter mission and its polarimetric and helioseismic imager (SO/PHI), *J. Phys.: Conf. Ser*. 271, 012086, doi: 10.1088/1742-6596/271/1/012086.

Gopalswamy, N., P. Mäkelä, H. Xie, S. Akiyama, and S. Yashiro (2009), CME interactions with coronal holes and their interplanetary consequences, *J. Geophys. Res.*, *114*, A00A22, doi: 10.1029/2008JA013686.

Guhathakurta, M., E. C. Sittler, and D. McComas (1999), Semi-empirical MHD model of the solar wind and its comparison with Ulysses, *Space Sci. Rev.*, *87*, 199-206.

Harvey, J. W., F. Hill, R. P. Hubbard, J. **R.** Kennedy, J. W. Leibacher, J. A. Pintar, P. A. Gilman, R. W. Noyes, A. M. Title, J. Toomre, R. K. Ulrich, A. Bhatnagar, J. A. Kennewell, W. Marquette, J. Patrón, O. Saá, E. Yasukawa (1996), The Global Oscillation Network Group (GONG) project, *Science*, *272*, 1284-1286, doi: 10.1126/science.272.5266.1284**.**

Hewish, A., P. F. Scott, and D. Wills (1964), Interplanetary scintillation of small diameter radio sources, *Nature*, *203*, 1214-1217, doi: 10.1038/2031214a0.

Issautier, K., R. M. Skoug, J. T. Gosling, S. P. Gary, and D. J. McComas (2001), Solar wind plasma parameters on Ulysses: Detailed comparison between the URAP and SWOOPS experiments, *J. Geophys. Res.*, *106*, 15665.

Jackson, B. V., P. L. Hick, M. Kojima, and A. Yokobe (1997), Heliospheric tomography using interplanetary scintillation observations, *Phys. Chem. Earth*, *22*, 425-434, doi: 10.1016/S0079-1946(97)00170-5.

Jackson, B. V., P. L. Hick, M. Kojima, and A. Yokobe (1998), Heliospheric tomography using interplanetary scintillation observations: 1. Combined Nagoya and Cambridge data, *J. Geophys. Res.*, *103*, 12049-12067, doi: 10.1029/97JA02528.

Jackson, B. V., P. P. Hick, A. Buffington, M. M. Bisi, J. M. Clover, M. Tokumaru, M. Kojima, and K. Fujiki (2011), Three-dimensional reconstruction of heliospheric structure using iterative tomography: A review, *J. Atoms. Sol. Terr. Phys.*, *73*, 1214 – 1227, doi:10.1016/j.jastp.2010.10.007.

Jackson, B. V., H.-S. Yu, A. Buffington, and P. P. Hick (2014), The dynamic character of the polar solar wind, *Astrophys. J.*, *79*, 54, doi: 10.1088/0004-637X/793/1/54.

Jian, L. K., C. T. Russell, J. G. Luhmann, P .J. MacNeice, D. Odstrcil, P. Riley, J. A. Linker, R. M. Skoug, and J. T. Steinberg (2011a), Comparison of observations at ACE and *Ulysses* with Enlil model results: Stream interaction regions during Carrington rotations 2016 – 2018, *Sol. Phys.*, *273*, 179-203, doi: 10.1007/s11207-011-9858-7.

Jian, L. K., C. T. Russell, and J. G. Luhmann (2011b), Comparing solar minimum 23/24 with historical solar wind records at 1 AU, *Sol. Phys.*, *274*, 321-344, doi: 10.1007/s11207-011-9737-2.

Jian, L. K., P. J. MacNeice, A. Taktakishvili, D. Odstrcil, B. Jackson, H.-S. Yu, P. Riley, I. V. Sokolov, and R. M. Evans (2015), Validation for solar wind prediction at Earth: Comparison of coronal and heliospheric models installed at the CCMC, *Space Weather*, *13*, 316-338, doi: 10.1002/2015SW001174.

Linker, J. A., Z. Mikić, and D. D. Schnack (1996), Global coronal modeling and space weather prediction, in *Solar Drivers of Interplanetary and Terrestrial Disturbances*, *ASP Conf. Ser.*, vol. 95, edited by K. S. Balasubramaniam, S. L. Keil, and R. N. Smartt, pp. 208-218, ASP, San Francisco, CA.

Linker, J. A., Z. Mikić, R. Lionello, P. Riley, T. Amari, and D. Odstrcil (2003), Flux cancellation and coronal mass ejections, *Phys. Plasmas*, *10*, 1971-1978, doi: 10.1063/1.1563668.

Lionello, R., J. A. Linker, and Z. Mikić (2009), Multispectral emission of the Sun during the first whole Sun month: Magnetohydrodynamic Simulations, *Astrophys. J., 690*, 902-912, doi: 10.1088/0004-637X/690/1/902.

Lee, C. O., J. G. Luhmann, D. Odstrcil, P. J. MacNeice, I. de Pater, P. Riley, and C. N. Arge (2009), The solar wind at 1 AU during the declining phase of solar cycle 23: Comparison of 3D numerical model results with observations, *Sol. Phys.*, *254*, 155-183, doi: 10.1007/s11207-008-9280-y.

Manchester, W. B., J. U. Kozyra, S. T. Lepri, and B. Lavraud (2014), Simulation of magnetic cloud erosion during propagation, *J. Geophys. Res.*, 119, 5499-5464, doi: 10.1002/2014JA019882.

MacNeice, P. (2009a), Validation of community models: Identifying events in space weather model timelines, *Space Weather, 7*, S06004, doi: 10.1029/2009SW000463.

MacNeice, P. (2009b), Validation of community models: 2. Development of a baseline using the Wang-Sheeley-Arge model, *Space Weather, 7*, S12002, doi: 10.1029/2009SW000489.

Mikić, Z., and J. A. Linker (1994), Disruption of coronal magnetic field arcades, *Astrophys. J., 430*, 898-912, doi: 10.1086/174460.

Mikić, Z., and J. A. Linker (1996), The large-scale structure of the solar corona and inner heliosphere, in *Solar Wind Eight*, *AIP Conf. Proc.*, vol. *382*, edited by D. Winterhalter, J. T. Gosling, S. R. Habbal et al., pp. 104-107, AIP, Woodbury, NY, doi: 10.1063/1.51370.

Müller, D., R. G. Marsden, O. C. St Cyr, and H. R. Gilbert (2013), Solar Orbiter: Exploring the Sun-Heliosphere Connection, *Sol. Phys.*, *285*, 25-70, doi: 10.1007/s11207-012-0085-7.

Odstrčil, D. (1994), Interaction of solar wind streams and related small structures, *J. Geophys. Res., 99*, 17653-17671, doi: 10.1029/94JA01225.

Odstrčil, D., and V. J. Pizzo (1999a), Three-dimensional propagation of coronal mass ejections (CMEs) in a structured solar wind flow 1. CME launched within the streamer belt, *J. Geophys. Res., 104*, 483-492, doi: 10.1029/1998JA900019.

Odstrčil, D., and V. J. Pizzo (1999b), Three-dimensional propagation of coronal mass ejections (CMEs) in a structured solar wind flow 2. CME launched adjacent to the streamer belt, *J. Geophys. Res.*, *104*, 493-503, doi: 10.1029/1998JA900038.

Odstrčil, D., M. Dryer, and Z. Smith (1996), Propagation of an interplanetary shock along the heliospheric plasma sheet, *J. Geophys. Res.*, *101*, 19973-19986, doi: 10.1029/96JA00479.

Oran, R., B. van der Holst, E. Landi, M. Jin, I. V. Sokolov, and T. I. Gombosi (2013), A global wave-driven magnetohydrodynamic solar model with a unified treatment of open and closed magnetic field topologies, *Astrophys. J.*, *778*, 176, 2013, doi: 10.1088/0004-637X/778/2/176.

Owens, M. J., C. N. Arge, H. E. Spence, and A. Pembroke (2005), An event-based approach to validating solar wind speed predictions: High-speed enhancements in the Wang-Sheeley-Arge model, *J. Geophys. Res., 110*, A12105, doi: 10.1029/2005JA011343.

Owens, M. J., H. E. Spence, S. McGregor, W. J. Hughes, J. M. Quinn, C. N. Arge, P. Riley, J. Linker, and D. Odstrcil (2008), Metrics for solar wind prediction models: Comparison of empirical, hybrid, and physics-based schemes with 8 years of L1 obsevations, *Space Weather, 6*, S08001, doi: 10.1029/2007SW000380.

Pierce, A. K. (1969), The solar program of the Kitt peak national observatory, *Sol. Phys., 6*, 498-503, doi: 10.1007/BF00146486.

Riley, P., J. A. Linker, and Z. Mikić (2001a), An empirically-driven global MHD model of the solar corona and inner heliosphere, *J. Geophys. Res.,* **106**, 15889-15901, doi: 10.1029/2000JA000121.

Riley, P., J. A. Linker, Z. Mikić, and R. Lionello (2001b), MHD modeling of the solar corona and inner heliosphere: Comparison with observations, in *Space Weather, Geophys. Monogr. Ser., vol. 125*, edited by P. Song, H. J. Singer, and G. L. Siscoe, pp. 159-167, AGU, Washington, D.C., doi: 10.1029/GM125p0159.

Riley, P., M. Ben-Nun, J. A. Linker, Z. Mikic, L. Svalgaard, J. Harvey, L. Bertello, T. Hoeksema, Y. Liu, and R. Ulrich (2014), A multi-observatory inter-comparison of line-of-sight synoptic solar magnetograms, *Sol. Phys., 289*, 769-792, doi: 10.1007/s11207-013-0353-1.

Schatten, K. H., J. M. Wilcox, and N. F. Ness (1969), A model of interplanetary and coronal magnetic fields, *Sol. Phys., 6*, 442-455, doi: 10.1007/BF00146478.

Scherrer, P. H., *et al*. (1995), The solar oscillation investigation - Michelson Doppler imager, *Sol. Phys., 162*, 129-188, doi: 10.1007/BF00733429.

Scherrer, P. H. *et al*. (2012), The Helioseismic and Magnetic Imager (HMI) investigation for the Solar Dynamics Observatory (SDO), *Sol. Phys., 275*, 207-227, doi: 10.1007/s11207-011-9834-2.

Sokolov, I. V., B. van der Holst, R. Oran, C. Downs, I. Roussev, M. Jin, W. B. Manchester, IV., R. M. Evans, and T. I. Gombosi (2013), Magnetohydrodynamic waves and coronal heating: Unifying empirical and MHD turbulence models, *Astrophys. J., 764*, 23, doi: 10.1088/0004-637X/764/1/23.

Tóth, G., I. V. Sokolov, T. I. Gombosi, D. R. Chesney, C. R. Clauer, D. L. De Zeeuw, K. C. Hansen, K. J. Kane, W. B. Manchester, R. C. Oehmke, K. G. Powell, A. J. Ridley, I. I. Roussev, Q. F. Stout, O. Volberg, R. A. Wolf, S. Sazykin, A. Chan, B. Yu, and J. Kóta (2005), Space weather modeling framework: A new tool for the space science community, *J. Geophys. Res., 110*, A12226, doi: 10.1029/2005JA011126.

Tóth, G., B. van der Holst, I. V. Sokolov, D. L. De Zeeuw, T. I. Gombosi, F. Fang, W. B. Manchester, X. Meng, D. Najib, K. G. Powell, Q. F. Stout, A. Glocer, Y.-J. Ma, and M. Opher (2012), Adaptive numerical algorithms in space weather modeling, *J. Comput. Phys.*, *231*, 870-903, doi: 10.1016/j.jcp.2011.02.006.

Ulrich, R. K., S. Evans, J. E. Boyden, and L. Webster (2002), Mount Wilson synoptic magnetic fields: improved instrumentation, calibration, and analysis applied to the 14 July 2000 flare and to the evolution of the dipole field, *Astrophys. J. Suppl., 139*, 259-279, doi: 10.1086/337948.

Usmanov, A. V., M. L. Goldstein, B. P. Besser, and J. M. Fritzer (2000), A global MHD solar wind model with WKB Alfvén waves: Comparison with Ulysses data, *J. Geophys. Res.*, *105* (A6), 12675-12695.

Vandas, M. and D. Odstrčil (2000), Magnetic cloud evolution: A comparison of analytical and numerical solutions, *J. Geophys. Res.*, *105*, 12605-12616, doi: 10.1029/2000JA900027.

van der Holst, B., W. B. Manchester, IV, R. A. Frazin, A. M. Vásquez, G. Tóth, and T. I. Gombosi (2010), A data-driven, two-temperature solar wind model with Alfvén waves, *Astrophys. J., 725*, 1373-1383, doi: 10.1088/0004-637X/725/1/1373.

van der Holst, B., I. V. Sokolov, X. Meng, M. Jin, W. B. Manchester, IV, G. Tóth, and T. I. Gombosi (2014), Alfvén wave solar model (AWSoM): Coronal heating, *Astrophys. J., 782*, 81, doi: 10.1088/0004-637X/782/2/81.

Wang, Y. M., and N. R. Sheeley, Jr. (1990a), Solar wind speed and coronal flux-tube expansion, *Astrophys. J., 355*, 726-732, doi: 10.1086/168805.

Wang, Y. M., and N. R. Sheeley, Jr. (1990b), Magnetic flux transport and the sunspot-cycle evolution of coronal holes and their wind streams, *Astrophys. J., 365*, 372-386, doi: 10.1086/169492.

Wang, Y. M., and N. R. Sheeley, Jr. (1992), On potential field models of the solar corona, *Astrophys. J., 392*, 310-319, doi: 10.1086/171430.

Wenzel, K. P., R. G. Marsden, D. E. Page, and E. J. Smith (1992), The Ulysses mission, *Astron. Astrophys. Suppl. Ser., 92*, 207-219.

Yu, H.-S., B. V. Jackson, Y.-H. Yang, N.-H. Chen, A. Buffington, and P. P. Hick (2016), 3D reconstruction of the polar jet of 17 June 2011 and its presence in the background solar wind, *J. Geophys. Res.*, in press.

Zhao, X., and J. T. Hoeksema (1995), Prediction of the interplanetary magnetic field strength, J. Geophys. Res., 100, 19–33, doi:10.1029/94JA02266.

Figure Captions

Figure 1. The orbit of Ulysses in the HGI coordinate system in 2007. *R* is the heliocentric distance. Magenta dashed horizontal lines in the second panel mark $\pm 60^{o}$ for the latitudinal limits of Enlil model. Red dashed vertical lines mark the pertinent segment of Ulysses orbit.

Figure 2. The coupling of synoptic magnetograms, coronal models, and heliospheric models to be validated with Ulysses observation. See text for denotations of acronyms. Because IPS tomography does not require magnetogram as input but only convects its field outward, their connection is marked by a dashed arrow line.

Figure 3. The comparison of two versions of Enlil model in reproducing Ulysses observations. Top row: Ulysses observation, middle row: GONG–WSA v2.2–Enlil v2.7, bottom row: GONG–WSA v2.2–Enlil v2.8. Left column: solar wind speed V (color bar: 250 – 850 km/s), middle column: IMF magnitude B (color bar: 0.63 – 10.0 nT on a logarithmic scale), right column: solar wind temperature Tp (color bar: 10.0 – 631 $\times 10^{3}$ K on a logarithmic scale). Each block is a stacked plot of seven CRs, with the abscissa for the day of each CR and the ordinate for CR 2056 to 2062.

Figure 4. The comparison of eight coupled corona-heliospheric models in reproducing the solar wind speed V (color bar: 250-850 km/s) at Ulysses orbit. Each block is a stacked plot of seven CRs, with the abscissa for the day of each CR and the ordinate for CR 2056 to 2062. The block with a color bar and in the black box shows the Ulysses data; the other blocks are results from different models. NSO stands for NSO/SOLIS hereafter.

Figure 5. The comparison of eight model combinations in reproducing the solar wind proton number density Np at Ulysses orbit. The caption of Figure 4 applies. The color bar marks Np of 0.5 – 31.6 $cm^{-3}$ on a logarithmic scale.

Figure 6. The comparison of seven model combinations in reproducing the IMF magnitude B at Ulysses orbit. The caption of Figure 4 applies. The color bar indicates B of 0.63 – 10.0 nT on a logarithmic scale.

Figure 7. The comparison of seven model combinations in reproducing the solar wind proton temperature Tp at Ulysses orbit. The caption of Figure 4 applies. The color bar indicates Tp of 10–631 $\times 10^{3}$ K on a logarithmic scale.

Figure 8. The comparison of eight model combinations installed at the CCMC and three persistence models in capturing the time series of solar wind parameters at Ulysses orbit during CRs 2056-2062. (A) RMSEs between simulation and observation for (a) V, (b) Np, (c) B, and (d) Tp. (B) RMSEs of solar wind parameters which have been first normalized by the averages in each CR: (a) V, (b) Np, (c) B, and (d) Tp. The ranking of the models is given at the bottom of each panel according to RMSE. The lower the RMSE, the higher is the ranking.

Figure 9. The distributions of occurrence with respect to the observed (abscissa) and modeled (ordinate) solar wind speed. The ranges in the abscissa and ordinate are the same. Color indicates the counts using the hourly data and ranges from 0 to 60. The bin size is 10 km/s. The cases with values higher than the last bin are counted in the last bin. The Pearson correlation coefficient between the observed and modeled solar wind speed is given at the top of each panel.

Figure 10. The caption of Figure 9 applies except this is for the solar wind proton number density. The bin size is 0.07 $cm^{-3}$.

Figure 11. The caption of Figure 9 applies except this shows the IMF magnitude B. The bin size is 0.06 nT.

Figure 12. The caption of Figure 9 applies except this shows the solar wind proton temperature. The bin size is 3500 K.

Figure 13. The distribution of solar wind speed (blue line) and IMF inward/outward polarity (orange line) versus the heliographic latitude from Ulysses observation and eight model combinations. The outward polarity is indicated by 1, inward by -1. The observation block is enclosed by a red box. The model names are given at the top of other blocks.

Figure 14. The ratios of mean (red dots) and median (blue dots) solar wind parameters between model results and observations (modeled/observed) for (a) V, (b) Np, (c) B, and (d) Tp within $\pm 30^o$ HGI latitude. The black dashed horizontal line in each panel indicates the ratio of 1.

Figure 15. The ratios of mean (red dots) and median (blue dots) solar wind parameters between model results and observations (modeled/observed) for (a) V, (b) Np, (c) B, and (d) Tp at HGI latitude $30^o$ – $60^o$ in the northern and southern hemispheres. The black dashed horizontal line in each panel indicates the ratio of 1.

Figure 16. The comparison of five different runs of GONG–WSA v2.2–Enlil v2.8 in reproducing solar wind speed at Ulysses orbit. The Ulysses data is shown in panel (d). Panel (a): the run using

fully calibrated CR synoptic maps and the present default setting at the inner boundary of Enlil model. Panels (b) and (e): runs using daily updated standard quick-reduce synoptic maps, with the present setting in (b) and an alternative setting in (e). Panels (c) and (f): runs using daily updated standard quick-reduce zero point corrected synoptic maps, with the present setting in (c) and an alternative setting in (f).

Figure 17. The caption of Figure 16 applies except this shows the solar wind proton density. The color bar marks Np of 0.5 – 31.6 $cm^{-3}$ on a logarithmic scale.

Figure 18. The caption of Figure 16 applies except this shows the IMF magnitude. The color bar marks B of 0.63 –10.0 nT on a logarithmic scale.

Figure 19. The comparison of GONG–WSA v2.2–Enlil v2.8 runs using three different magnetogram synoptic maps in reproducing the IMF inward/outward polarity observed by Ulysses. Yellow for inward, brown for outward. Left: without IMF sector grouping. Right: with IMF sector grouping requiring one sector to last at least one day. Panels (a) and (e): Ulysses observation, panels (b) and (f): using integral CR synoptic maps, panels (c) and (g): using daily updated standard quick-reduce synoptic maps, panels (d) and (h): using daily updated standard quick-reduce zero point corrected synoptic maps.

Figure 20. The comparison of five different runs of GONG–WSA v2.2–Enlil v2.8 in capturing the time series of solar wind parameters at Ulysses orbit during CRs 2056-2062: (1) using CR synoptic maps and the present default setting at the inner boundary of Enlil, (2) using daily updated synoptic maps and the present setting of Enlil, (3) using daily updated zero point corrected maps and the present setting of Enlil, (4) using daily updated synoptic maps and an alternative setting at the inner boundary of Enlil, (5) using daily zero point corrected maps and the same alternative setting of Enlil. RMSEs between simulation and observation for (a) V, (b) Np, (c) B, and (d) Tp. The ranking of the models is given at the bottom of each panel according to RMSE. The lower the RMSE, the higher is the ranking. The parameter scales are set the same as in Figure 8 (A) for comparison.

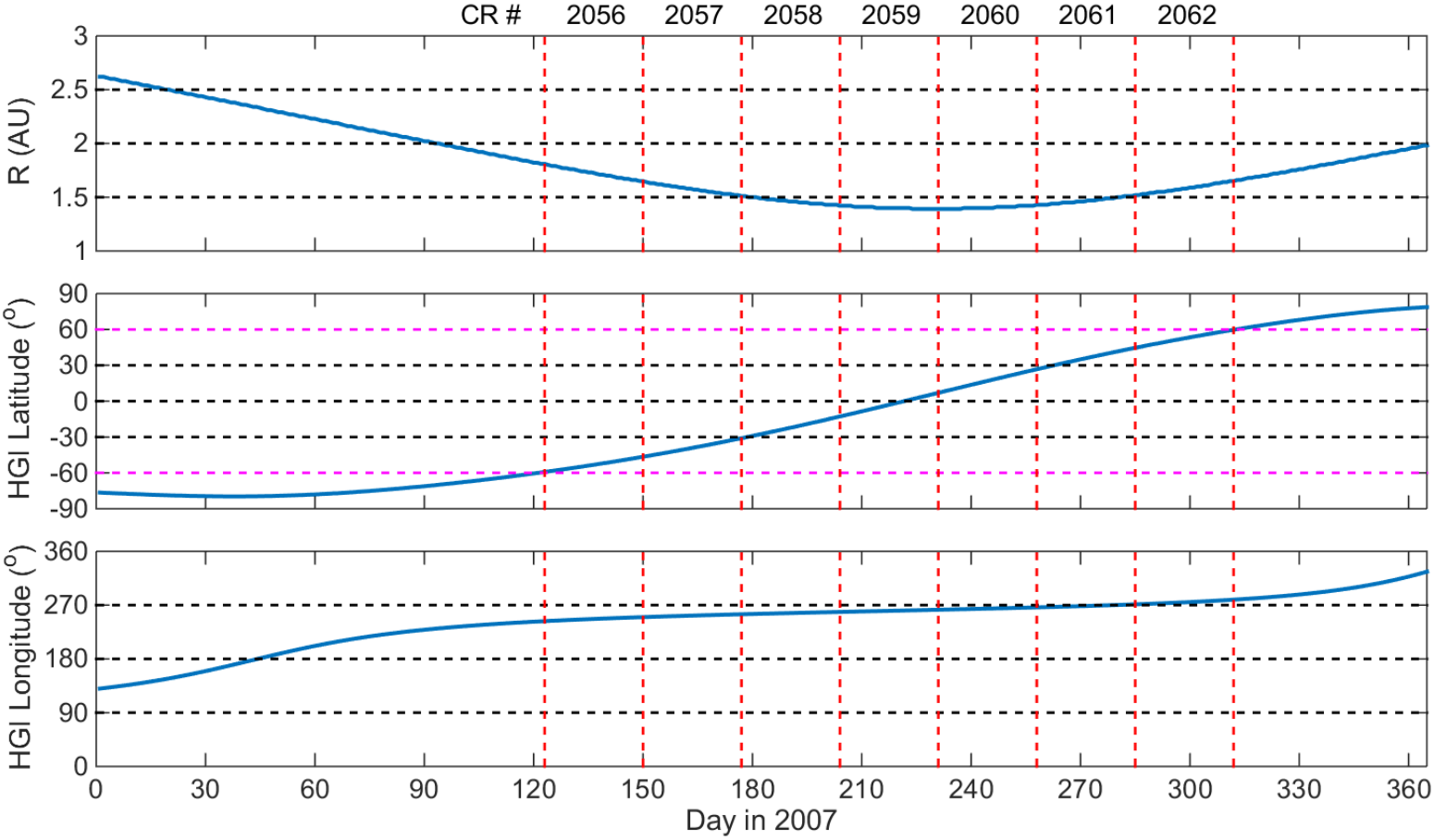


2016SW001435-f01-z-.tif

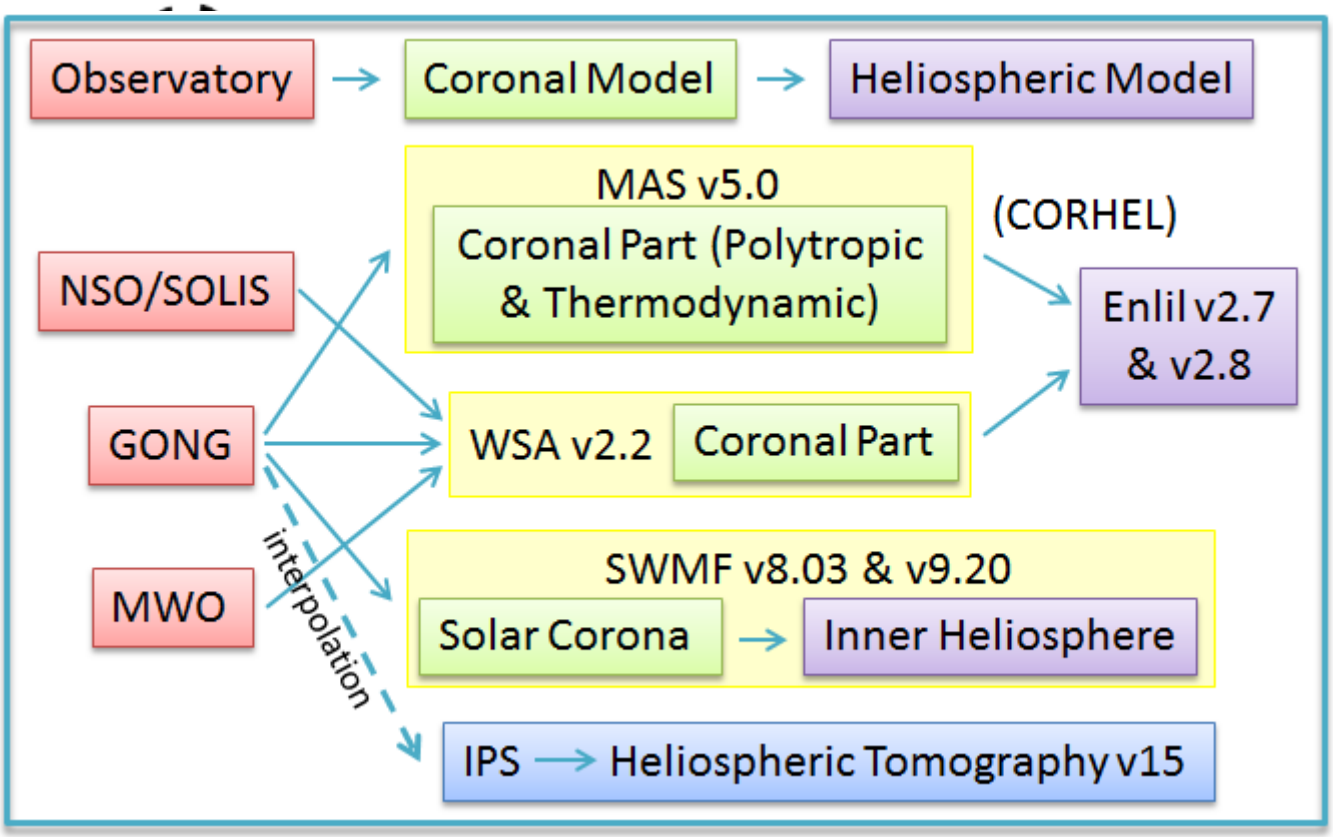


2016SW001435-f02-z-.tif

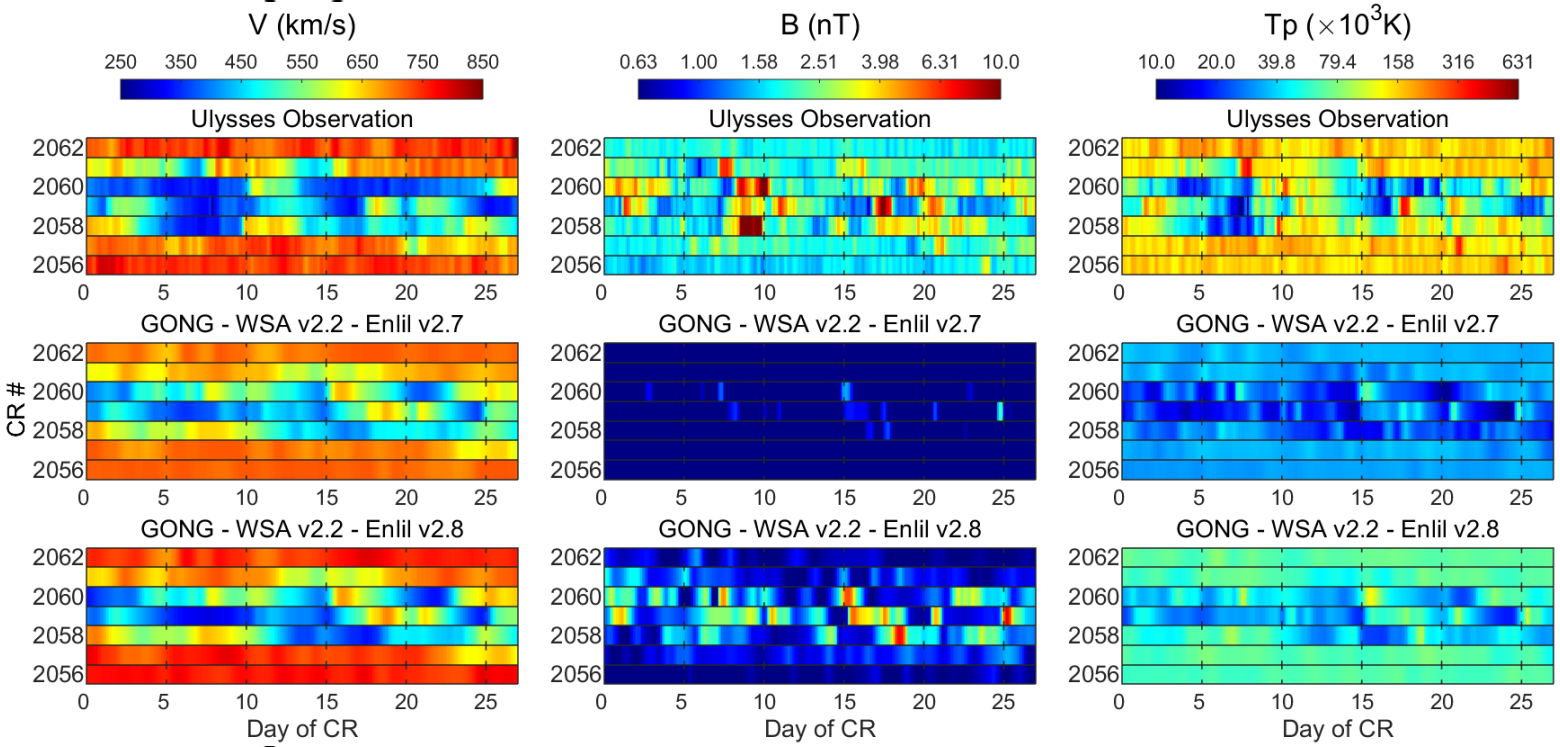


2016SW001435-f03-z-.tif

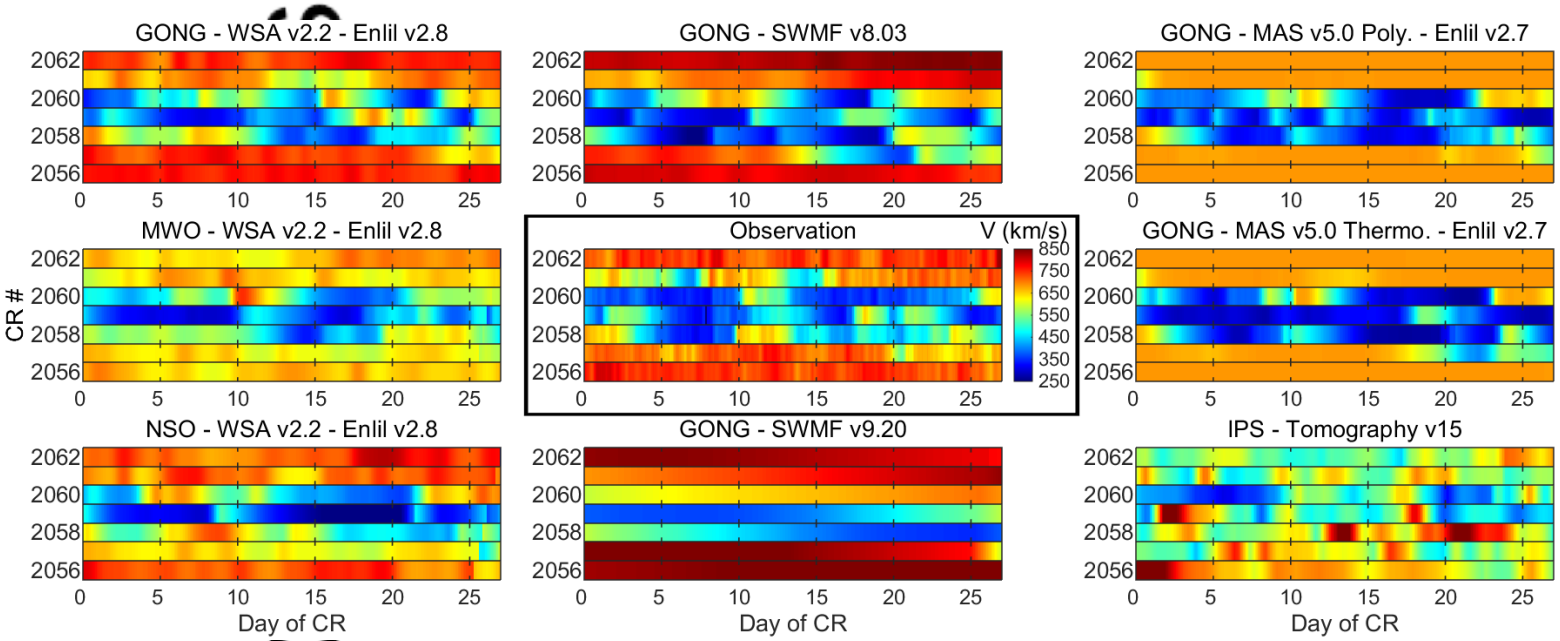


2016SW001435-f04-z-.tif

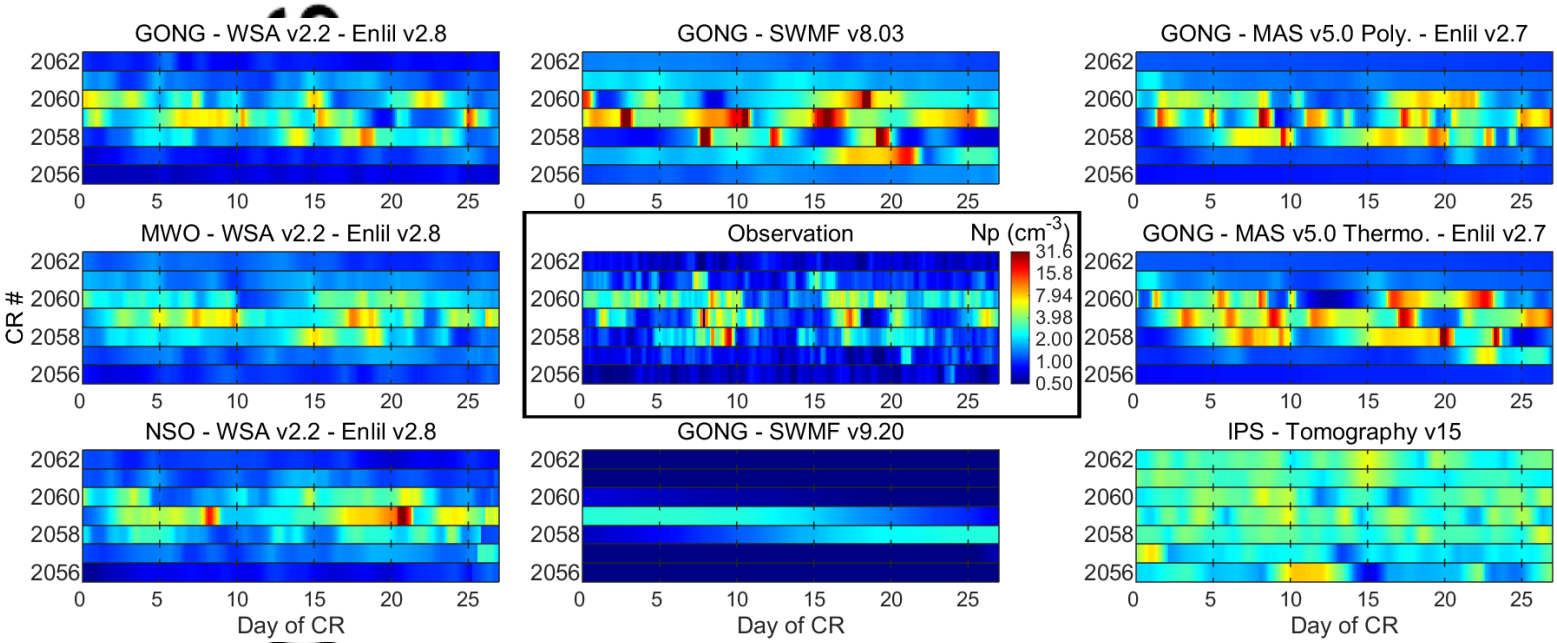


2016SW001435-f05-z-.tif

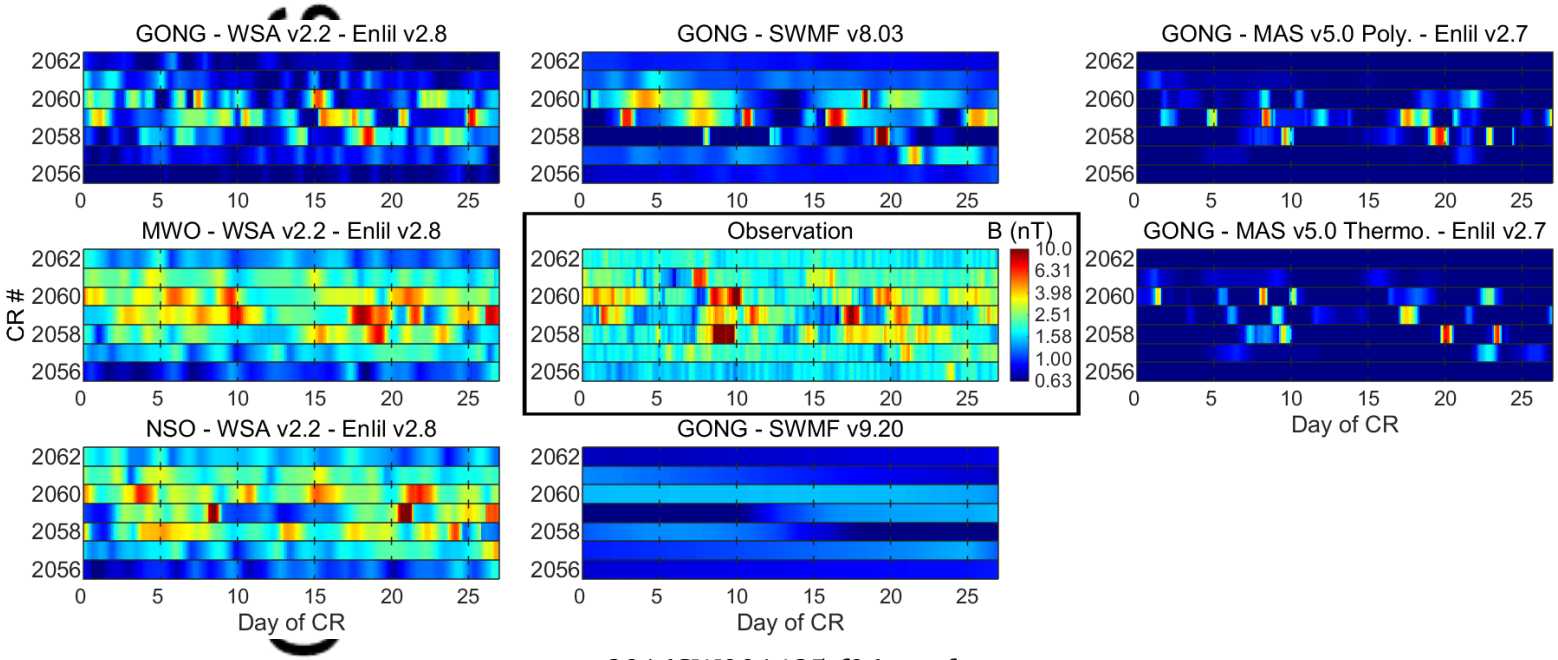


2016SW001435-f06-z-.tif

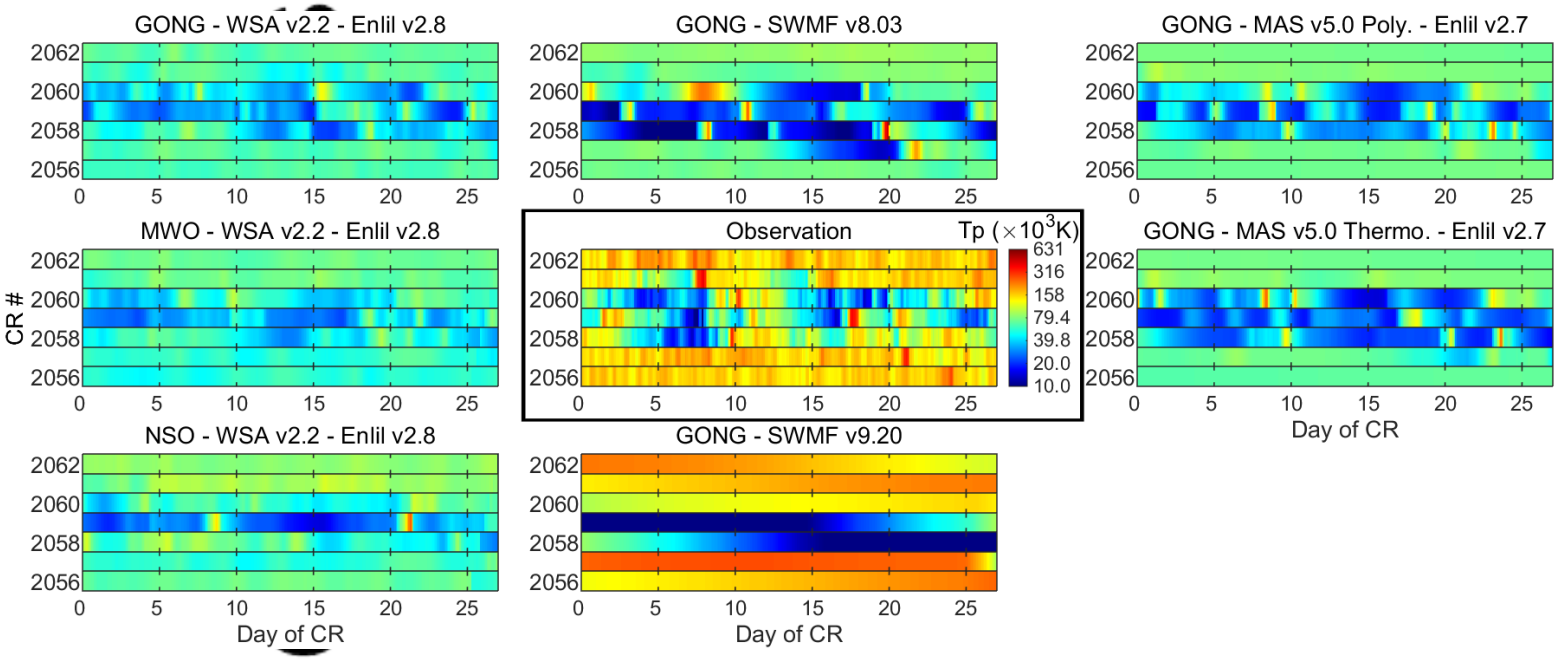


2016SW001435-f07-z-.tif

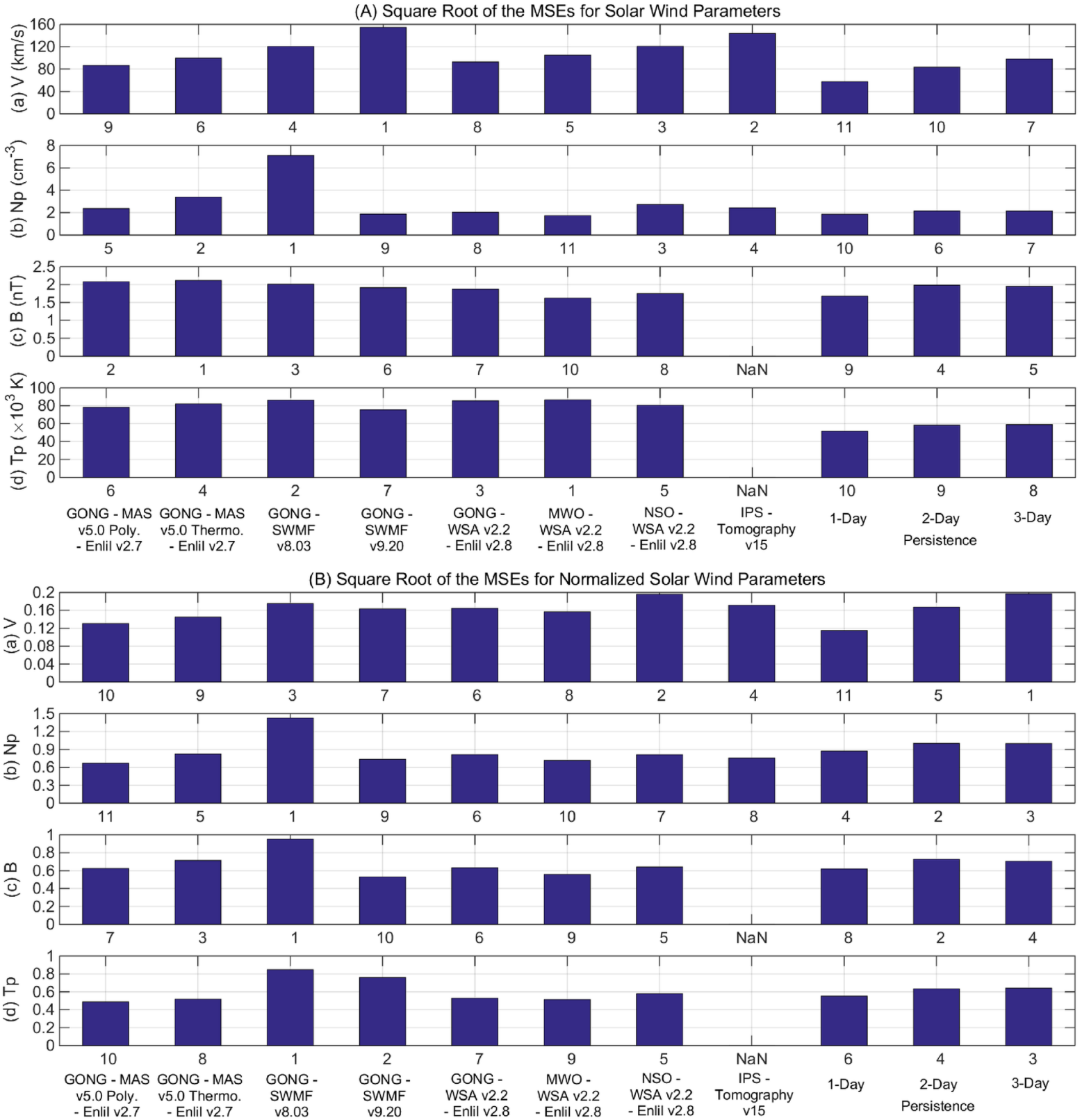


2016SW001435-f08-z-.tif

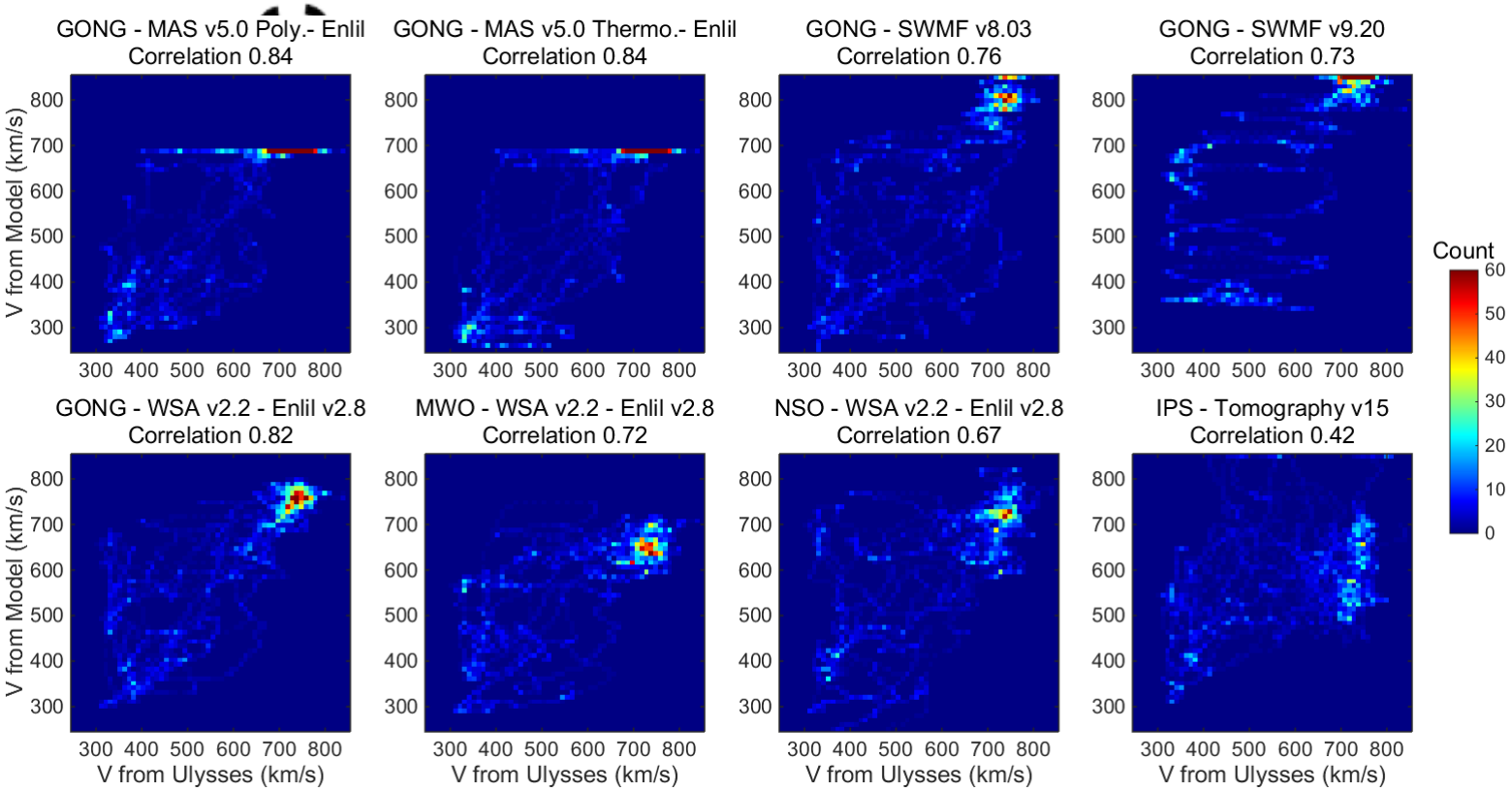


2016SW001435-f09-z-.tif

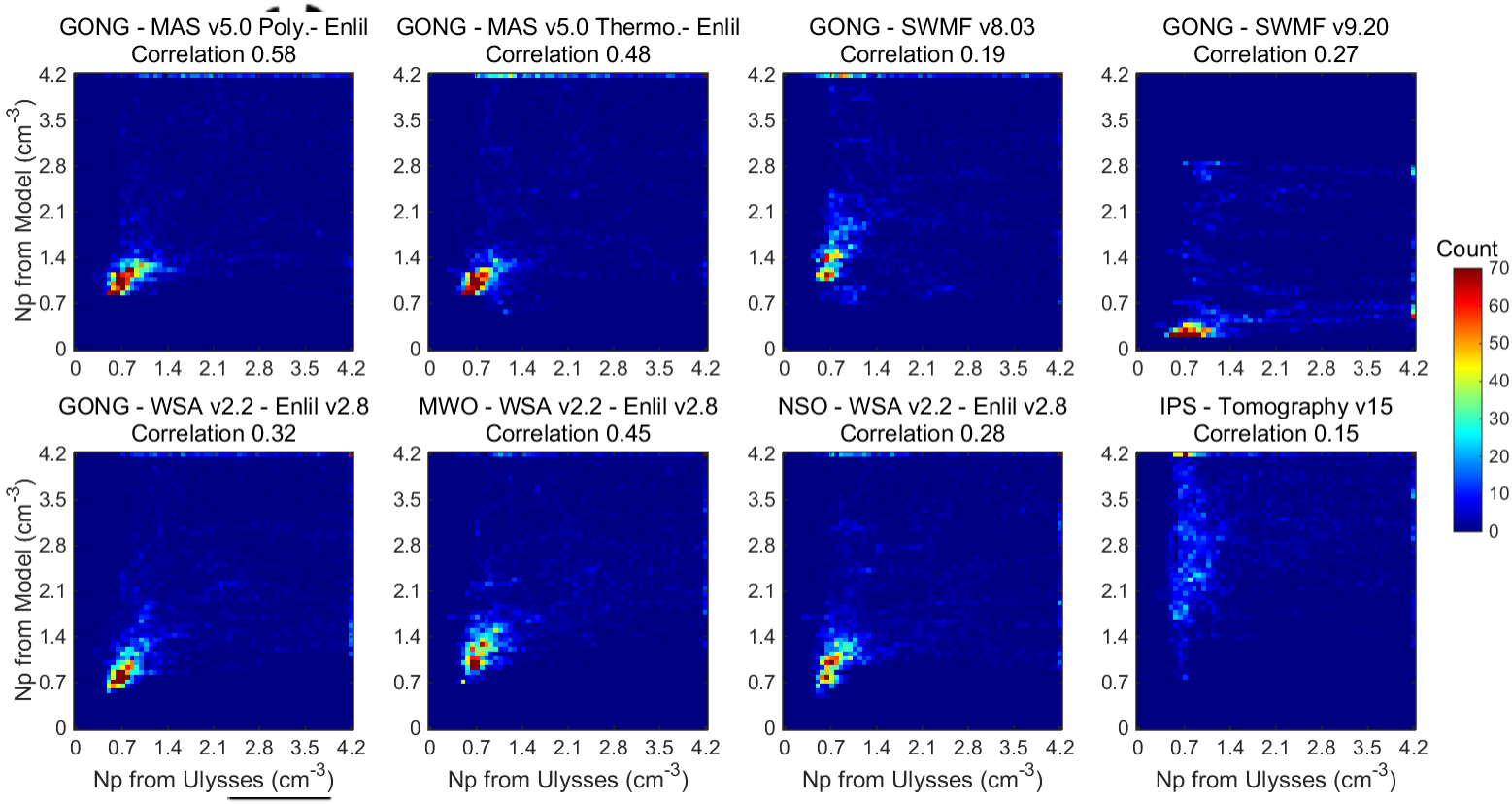


2016SW001435-f10-z-.tif

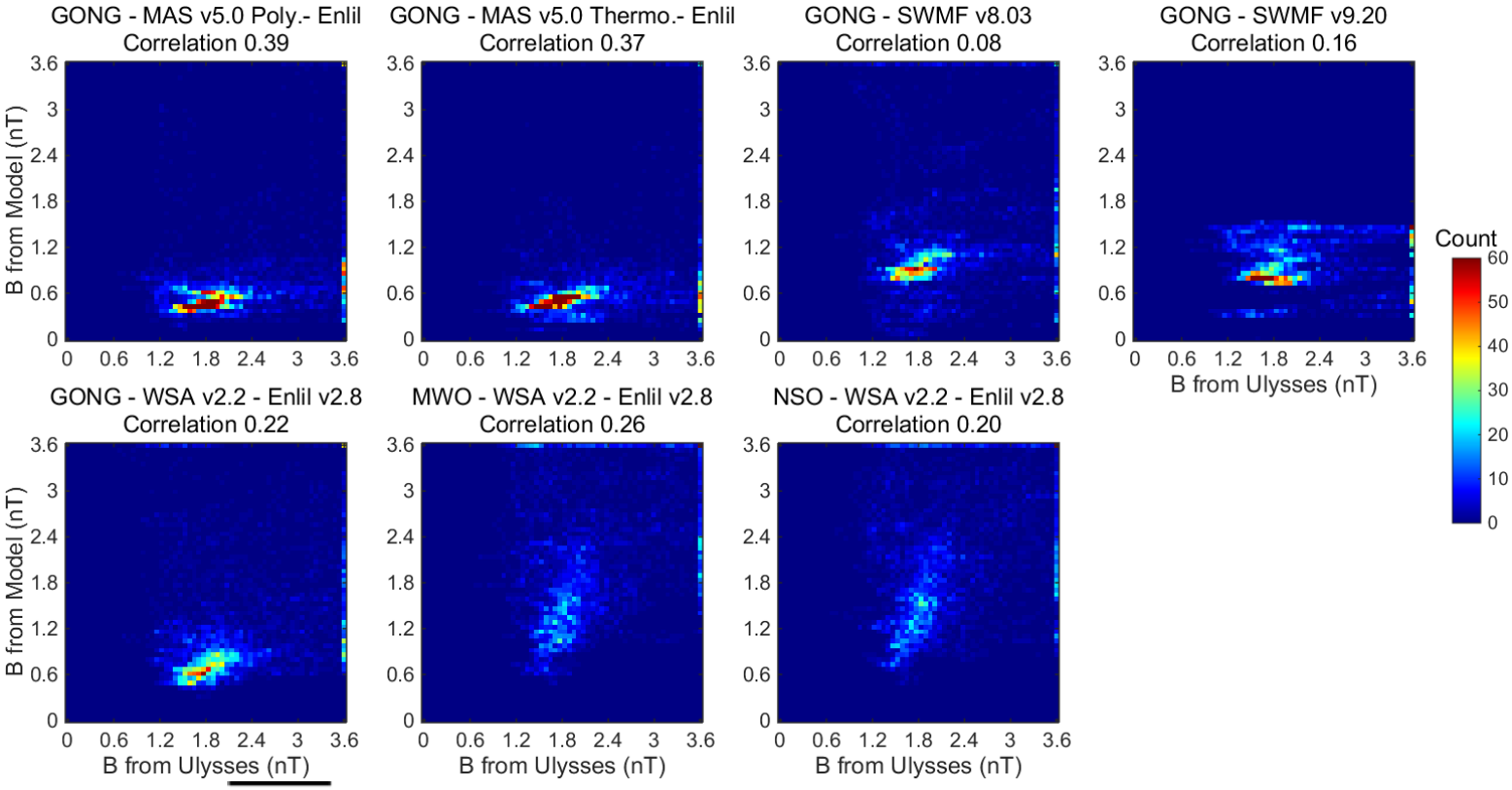


2016SW001435-f11-z-.tif

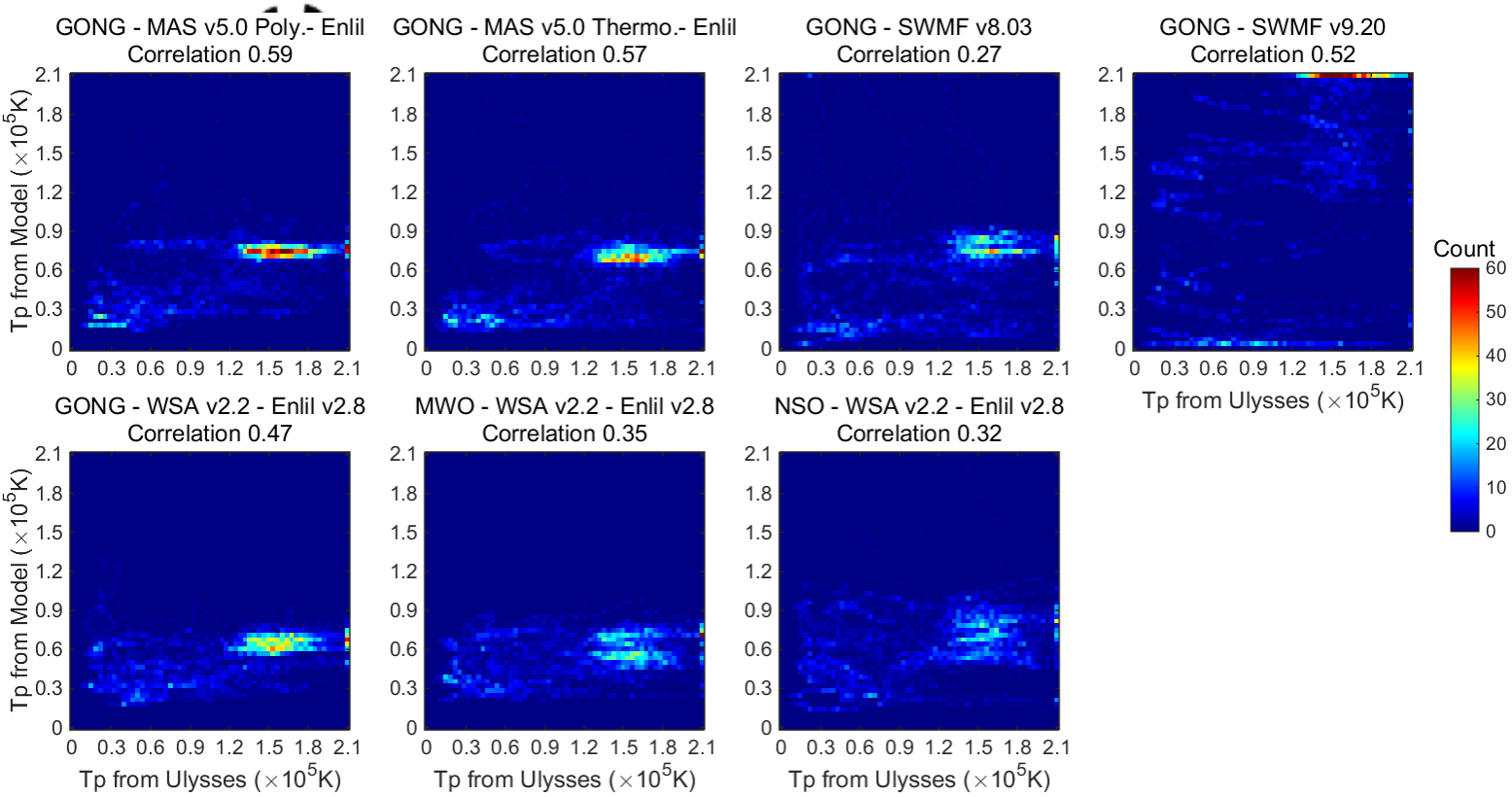


2016SW001435-f12-z-.tif

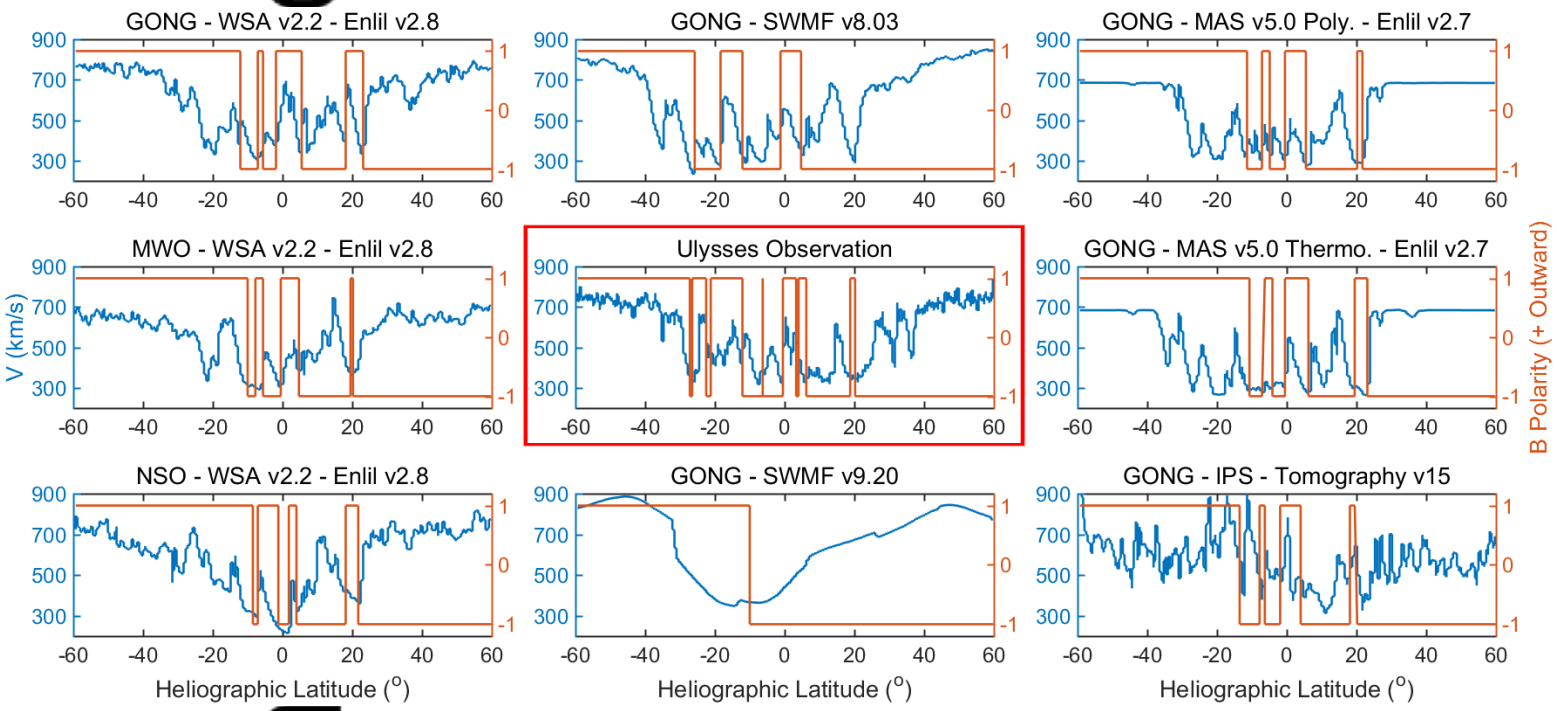


2016SW001435-f13-z-.tif

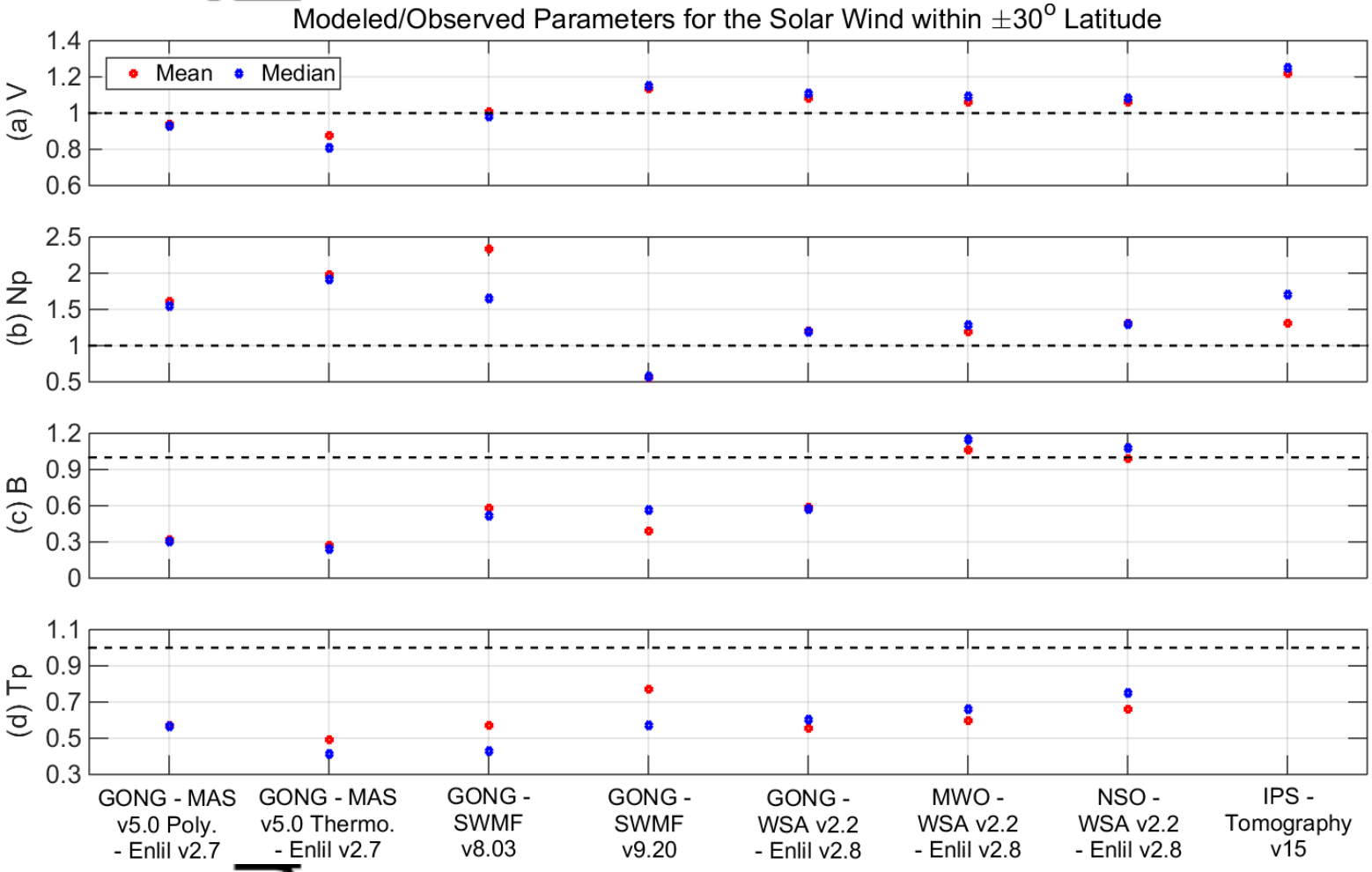


2016SW001435-f14-z-.tif

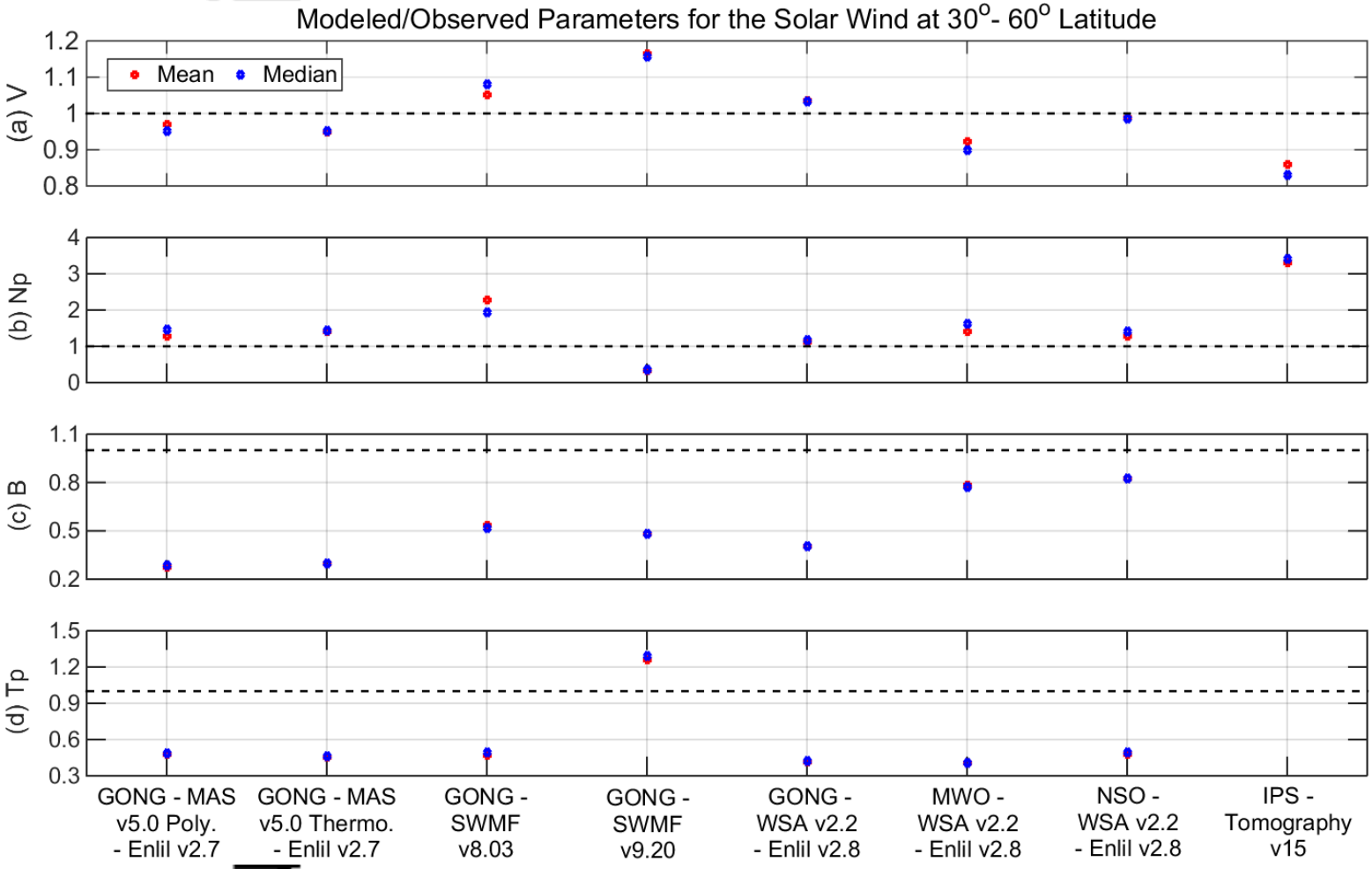


2016SW001435-f15-z-.tif

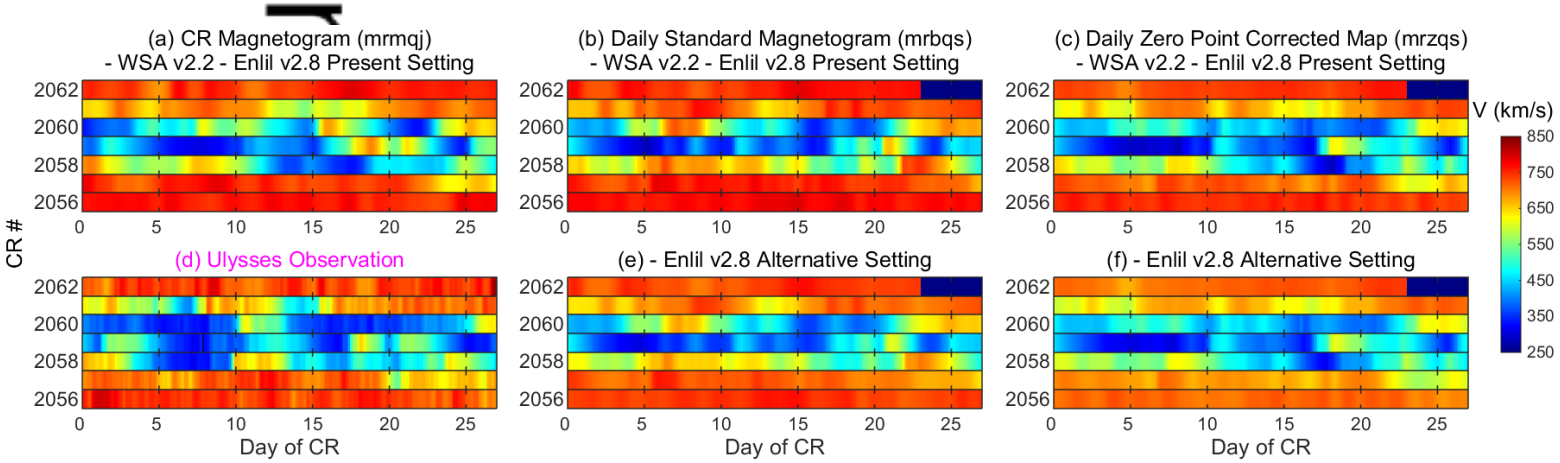


2016SW001435-f16-z-.tif

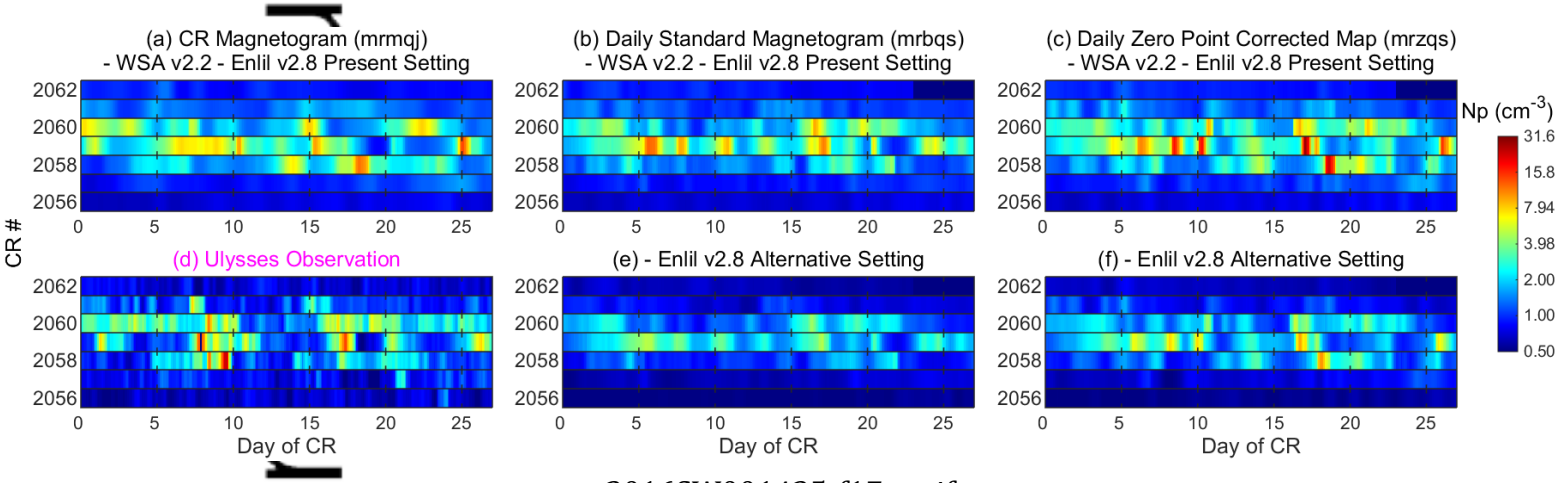


2016SW001435-f17-z-.tif

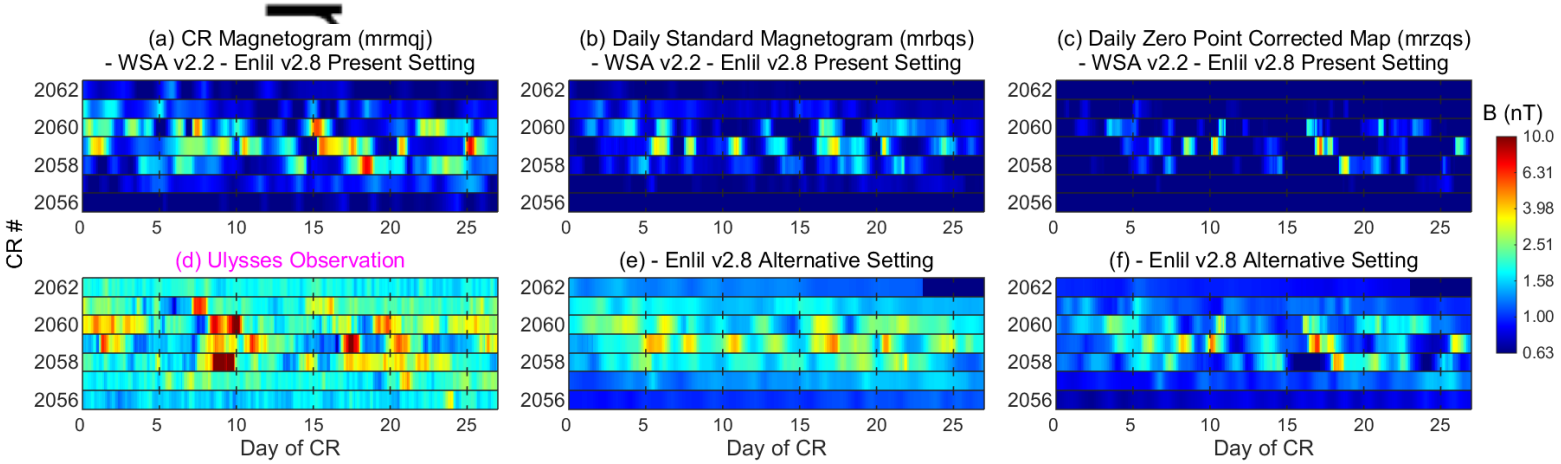


2016SW001435-f18-z-.tif

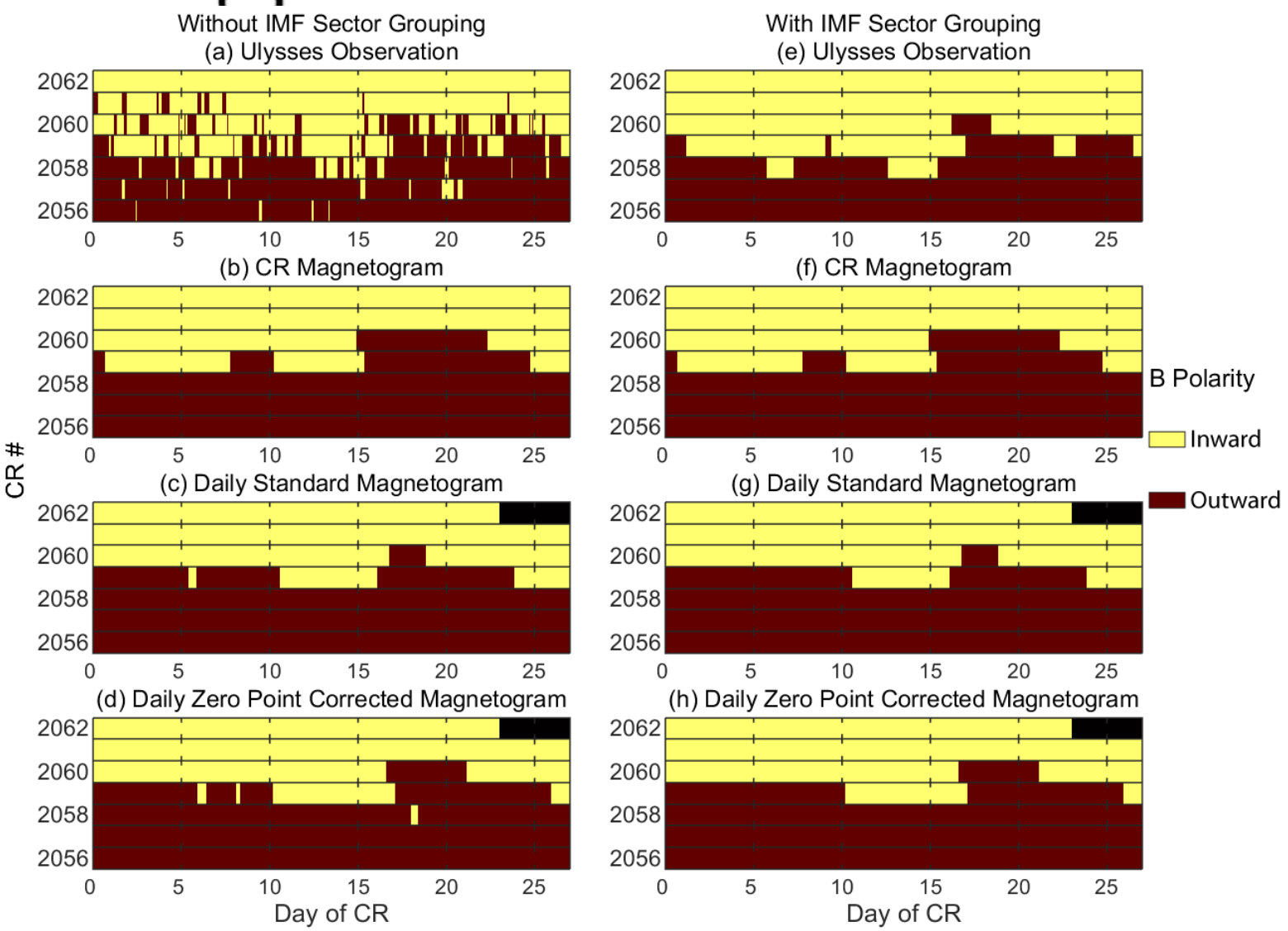


2016SW001435-f19-z-.tif

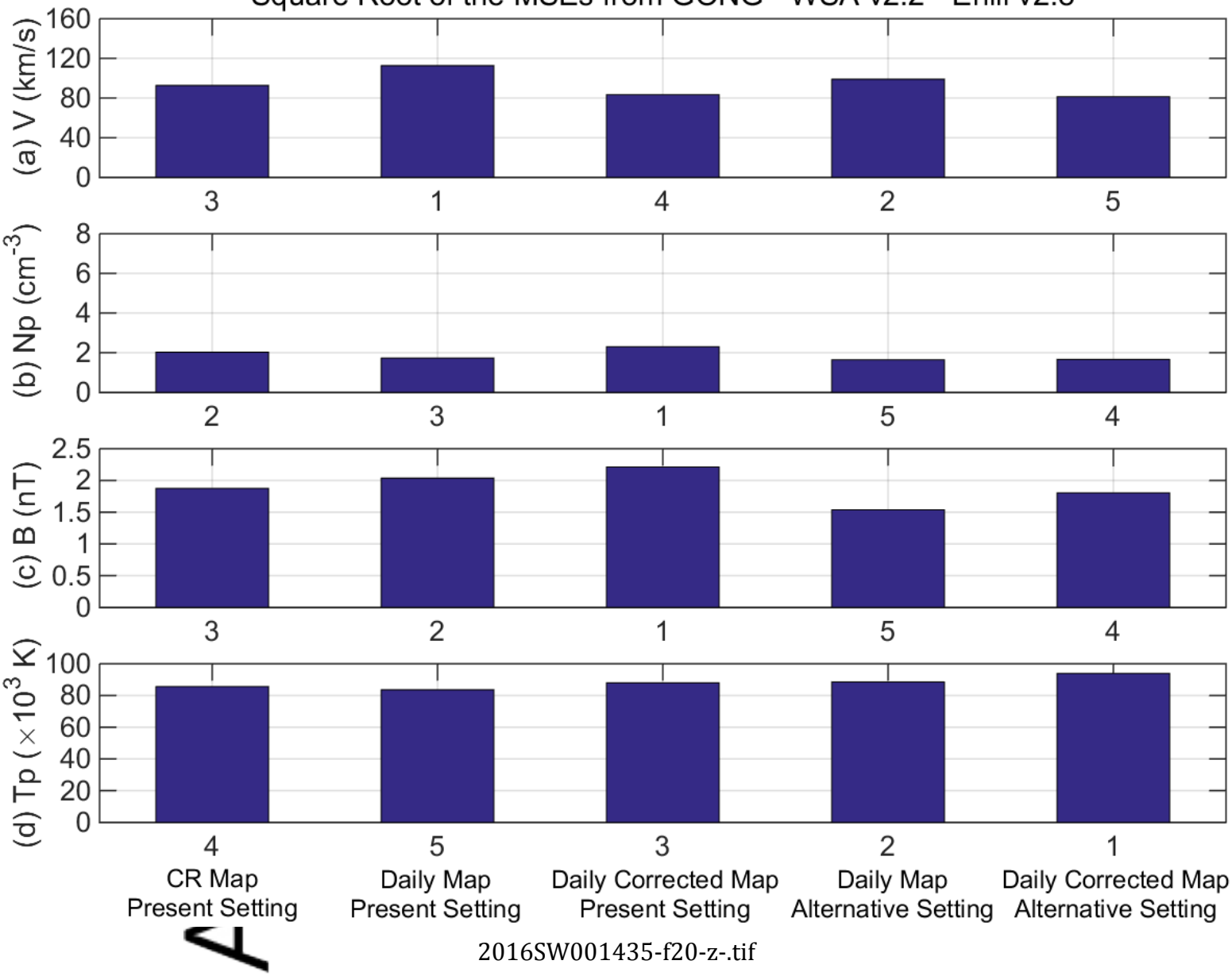


2016SW001435-f20-z-.tif

Table 1. Introduction of Models

| Model | Description | | | Resolution | | Inner Boundary Condition |
|---|---|---|---|---|---|---|
| WSA v2.2 coronal part, up to 21.5 Rs | PFSS+Schattern current sheet model, semi-empricial | | | Magnetogram with a smoothed resolution of $2.5^o$ in lat. & longitude | 101×92×182 (radial × latitude × longitude) → (0.20Rs, $2.0^o$, $2.0^o$) | Radial surface field, magnitude is set so that its line of sight component matches magnetogram |
| MAS v5.0 coronal part, up to 30 Rs | 3-D MHD model | Polytropic | Zero beta approximation | Magnetogram with a resolution of $1^o$ in latitude and longitude | 101×101×128 → (0.29Rs, $1.8^o$, $2.8^o$) | Base of corona: T=1.8MK, $N=2\times10^8 cm^{-3}$ |
| | | Thermo-dynamic | Full thermodynamic energy equation | | 151×101×182 → (0.19Rs, $1.8^o$, $2.0^o$) | Chromosphere: T=0.02MK, $N=2\times10^{12} cm^{-3}$ |
| Enlil heliospheric model, up to 430 Rs | 3-D MHD model for super-Alfvenic solar wind, driven by WSA, MAS, and possibe by other models too, only one temperature | | | v2.8, couping with WSA | 1024×120×360 → (0.40Rs, $1.0^o$, $1.0^o$) | 21.5 Rs: $V_{slow}$=200km/s, $V_{fast}$=700km/s, T=2MK, $N=200 cm^{-3}$ |
| | | | | v2.7, coupling with MAS | 320×60×180 → (1.25Rs, $2.0^o$, $2.0^o$) | 30 Rs: $V_{slow}$=250km/s, $V_{fast}$=650km/s, T=0.6MK, $N=150 cm^{-3}$ |
| SWMF, 3-D MHD model, up to 500 Rs, separate ion and electron temperatures | v8.03 | Starting from corona, semi-empricial solar wind heating | | Non-uniform grid. Within 24 Rs: cell size ranging 0.025-0.75 Rs. Heliospheric part (starting at 20 Rs): a minimum cell size of 1 Rs | | Top of chromosphere: T=0.02MK, $N= 2\times10^{10}$ $cm^{-3}$ |
| | v9.20 | Starting from the upper chromosphere, adding physics-based turbulent Alfven wave dissipation for coronal heating and solar wind acceleration | | Non-uniform grid. Inside 1.7 Rs: the angular resolution of $1.4^o$. Coronal part (chromosphere to 24 Rs): cell size ranging 0.001-0.8 Rs. Heliospheric part: 2 Rs within the current sheet, 8 Rs elsewhere (higher resolution of 1 Rs within the current sheet in a new refinement which is in progress) | | Top of chromosphere: T=0.05MK, $N=2\times10^{11}$ $cm^{-3}$ |
| IPS tomography v15 | 3-D reconstuction using a kinematic solar wind model and tomographically fitting it to IPS observation | | | Time cadence of 6 h (can be increased to 3 h after using more worldwide IPS data) | | N/A |

Table 2. Summary of the Model Evaluation Using Ulysses Comparison in May - November of 2007

| Synoptic map | Model | | Strength | | | Weakness | | |
|---|---|---|---|---|---|---|---|---|
| | SC part | IH part | | | | | | |
| MWO | WSA v2.2 | Enlil v2.8 | lowest RMSE for Np and B | match well with median B at all latitudes | match well with median Np at all latitudes | underestimate the fast wind V at mid-high latitudes | | |
| NSO/ SOLIS | | | best match for low-lat median B and Tp, and high-lat median V | | | largest RMSE for normalized V, second least correaltion with V | | |
| GONG | | | second highest correlation for V | | | N/A | | under-estimate B at all latitudes |
| | MAS v5.0 Polytropic | Enlil v2.7 | lowest RMSE for V, normalized V, Np, and Tp; highest correlation for Np, B, and Tp | | highest correlation for V | N/A | underestimate the fast wind V at mid-high latitudes; overestimate low-lat median Np | |
| | MAS v5.0 Thermo-dynamic | | second lowest RMSE for normalized V; second highest correlation for Np, B, and Tp | | | overestimate low-lat median Np most, underestimate low-lat median B and Tp most | | |
| | SWMF v8.03 | | match low-lat median V best | | | largest RMSE for Np, normalized Np, B, and Tp; lowest correlation for B and Tp | | |
| | SWMF v9.20 | | capture the high-lat hot solar wind well; lowest RMSE for Tp and normalized B | | | latitudinal variations are much smoothed; produce north-south asymmetry not observed by Ulysses; largest RMSE for V | | |
| IPS Tomography v15 | | | N/A | | | produce transient structures not observed by Ulysses at mid-high latitudes; could not capture the latitudinal variation of Np; lowest correlation for V and Np; mismatch high-lat median V and Np most | | |